Tellus SERIES A DYNAMIC METEOROLOGY AND OCEANOGRAPHY
PUBLISHED BY THE INTERNATIONAL METEOROLOGICAL INSTITUTE IN STOCKHOLM

Mesoscale cyclogenesis over the western North Pacific Ocean during TPARC

By CHRISTOPHER A. DAVIS[1]*, SARAH C. JONES[2], DORIS ANWENDER[2], JANINA BADEY[2] and LEONHARD SCHECK[2], [1]*National Center for Atmospheric Research, Boulder, Colorado, USA*; [2]*Karlsruhe Institute of Technology, Karlsruhe, Germany*

(Manuscript received 25 April 2012; in final form 15 December 2012)

ABSTRACT

Three cases of mesoscale marine cyclogenesis over the subtropics of the Western Pacific Ocean are investigated. Each case occurred during the THORPEX Pacific Asia Regional Campaign and Tropical Cyclone Structure (TCS-08) field phases in 2008. Each cyclone developed from remnants of disturbances that earlier showed potential for tropical cyclogenesis within the tropics. Two of the cyclones produced gale-force surface winds, and one, designated as a tropical cyclone, resulted in a significant coastal storm over eastern Japan. Development was initiated by a burst of organized mesoscale convection that consolidated and intensified the surface cyclonic circulation over a period of 12–24 h. Upper-tropospheric potential vorticity anomalies modulated the vertical wind shear that, in turn, influenced the periods of cyclone intensification and weakening. Weak baroclinicity associated with vertical shear was also deemed important in organizing mesoscale ascent and the convection outbreaks. The remnant tropical disturbances contributed exceptional water vapour content to higher latitudes that led to strong diabatic heating, and the tropical remnants contributed vorticity that was the seed of the development in the subtropics. Predictability of these events more than three days in advance appears to be minimal.

Keywords: tropical cyclone, T-PARC, mesoscale cyclone, vertical shear, moist convection

1. Introduction

During the warm season over tropical and warm subtropical waters, most interests focus on the formation of tropical cyclones. It is well known that the remnants of tropical cyclones can instigate renewed cyclogenesis, generally termed extratropical transition, if they reach higher latitudes under favourable synoptic-scale flow configurations (Jones et al., 2003). However, most tropical disturbances do not become tropical cyclones. Track climatologies indicate that the vast majority of tracks of non-developing disturbances remain in the tropics and are an important part of the annual rainfall where they reach land (Hennon et al., 2011). Yet, some of these disturbances reach the subtropics and even mid-latitudes where the high tropical moisture content, coupled with baroclinicity, can create a thermodynamically unstable state and a large convective response. Associated with this convection can be mesoscale cyclogenesis.

The term 'mesoscale cyclone' is representative of numerous phenomena that are well studied, including tropical cyclones. These have appreciable wind perturbations well constrained within a deformation radius from their circulation centre. These include mesoscale vortices (or mesoscale convective vortices, MCVs), mesoscale frontal cyclones and polar lows. While frontal cyclones can arise purely from baroclinic processes, or mixed barotropic and baroclinic instability, systems that remain entrenched within the mesoscale and do not benefit from diabatic heating seldom achieve appreciable intensity. This is because the deep systems that rely on baroclinic energy conversions occur on the synoptic-scale, that is, with wavelengths of typically 4000 km or more. Diabatic effects, primarily in the form of latent heat release in deep moist convection, give rise to a broader spectrum of disturbances. Diabatic Rossby-waves or diabatic Rossby-vortices (Parker and Thorpe, 1995; Wernli et al., 2002, Moore and Montgomery, 2004; Conzemius et al., 2007, Boettcher and Wernli, 2012) and MCVs (Bartels and Maddox, 1991) are mesoscale cyclones

*Corresponding author.
email: cdavis@ucar.edu
The National Center for Atmospheric Research is sponsored by the National Science Foundation.

Citation: Tellus A 2013, **65**, 18621, http://dx.doi.org/10.3402/tellusa.v65i0.18621

that arise in sheared flows, but whose primary energy source is latent heat release.

Because the spatial scale of mesoscale cyclones is small compared to baroclinic waves,[1] their time scales tend to be short also. For instance, the typical time scale for MCVs is one day or less. Formation occurs in roughly 6 hours within an area of organized convection that is typically 200–400 km in spatial extent. Unless convection can be maintained or recur, the vortex usually decays within 12–24 h. Diabatic Rossby-waves or vortices can have a lifetime of several days if moisture is abundant, baroclinicity is maintained and deformation remains modest. They can also project onto tropospheric-deep baroclinic modes.

A central question about mesoscale cyclogenesis, as it pertains to tropical cyclone formation, is the mechanism that creates a strong, swirling, surface wind field. These winds are important for further amplification of the vortex by air–sea fluxes of heat and water vapour. Yet, the traditional view of organized deep convection is that it produces cyclonic vorticity and potential vorticity (PV) in the middle-troposphere due to the presence of mesoscale downdrafts and associated near-surface divergence. Downdrafts and the associated diabatic cooling favour anticyclonic vorticity and negative PV anomaly tendencies in the lowest 1–3 km. These tendencies inhibit the intensification of cyclonic vorticity. Therefore, studies have noted the need for multiple cycles of deep convection that modify the diabatic heating profile and favour vorticity formation at the surface (Raymond et al., 1998; Dunkerton et al., 2009).

The topic of this article, however, is the formation of strong mesoscale surface cyclones in a single burst of organized convection. The term 'burst' refers to a cycle of mesoscale convection, which lasts roughly 12–24 h and produces a cold cloud shield that covers an area roughly 200–400 km across. We assert that this process occurred in several instances during the THORPEX Pacific Asia Regional Campaign (TPARC) which was conducted between August and September, 2008. Herein we focus on three cases that were generally well documented by research aircraft and for which operational numerical products provide information to guide the interpretation of the processes involved.

Three events, occurring between 30 August and 11 September, each represent mesoscale surface cyclogenesis following somewhat different phenomenological pathways. One of these was deemed a tropical cyclone that formed near 30°N (named 16W) according to the Joint Typhoon Warning Center (JTWC). The others had evidence of developing frontal structure and highly asymmetric wind fields and were not designated as tropical cyclones even though one of them had sustained surface winds of at least 20 ms^{-1}.

The goal of this article is to utilize various information sources to confirm the existence of the mesoscale cyclones, document the environments in which they occur and infer the mechanism(s) governing their formation. We also aim to link these phenomena to subtropical cyclones and the genesis stage of tropical cyclones.

2. Data and methods

The data used in this study consist of analyses and forecasts from the European Centre for Medium-range Weather Forecasting (ECMWF), obtained as part of the Year of Tropical Convection (YOTC) extensive archive (Waliser and Moncrieff, 2008; Chakraborty, 2010). Both operational analyses and forecasts are used herein, with the additional tendency fields provided as part of the YOTC data stream constituting an important part of the analysis. The horizontal grid increment of both analyses and forecasts is 25 km, and the vertical grid spacing is 25 hPa in pressure coordinates. The version of the model was *33r1* implemented in June, 2008.[2]

Three-hourly data from the ECMWF forecast model allow for the computation of area-mean tendencies of physical processes in the model. Variables include temperature tendencies due to parameterized convection, grid-resolved condensation, three-dimensional advection and adiabatic temperature changes, short-wave radiation, long-wave radiation and turbulent diffusion and fluxes. This output also proves sufficient to compute vorticity budgets using the method outlined in Davis and Galarneau (2009, see their equation 4). Budgets are computed using system-relative winds in a system-following coordinate. Vorticity tendencies due to stretching, eddy fluxes into or out of the box, tilting effects and friction are computed as a function of time and pressure. In order to establish the sensitivity to the box location (and hence to small perturbations on the edge of the box), an ensemble of budgets is computed following Davis and Galarneau (2009) in which the box is varied over a $\pm 1^{\circ}$ range in 0.25° increments, yielding 81 ensemble members. The final budget is the mean of the ensemble and the standard deviation of the ensemble indicates the uncertainty in budget terms.

[1]While comparison of the scale of isolated vortices to synoptic-scale waves is not straightforward, an approximate vortex scale is the e-folding radius of the tangential velocity, which for mesoscale vortices, including tropical cyclones, is typically 100–200 km. This may be compared with ¼ of a wavelength of a baroclinic wave, or approximately 1000 km.

[2]Details are available at http://www.ecmwf.int/research/ifsdocs/CY33r1/index.html

Data from two flights of the DLR Falcon are also used in the analysis herein. Both dropsondes and water vapour lidar measurements are incorporated. The dropsondes are processed through the ASPEN software at NCAR as the primary quality control step. The vertical resolution of the dropsondes data is approximately 10 m, but these data are converted to 5 hPa in pressure coordinates plus the lowest dropsonde level above the surface. Time–space correction of the dropsondes data is included in the third case only. Dropsonde positions are assigned to the spatial location at 700 hPa without correction for drift.

Observations from both the SeaWinds scatterometer aboard the NASA Quick Scatterometer satellite (termed QuikSCAT, Atlas et al., 2001) and the Advanced Scatterometer (ASCAT), operated by the European Organization for the Exploitation of Meteorological Satellites (EUMESAT), are used to define the position, structure and intensity of the cyclones near the surface. Individual swaths are processed separately. Quality control flags present in the data are used to indicate wind retrievals of questionable validity and the presence of rain. Rain does not necessarily render data questionable. Visual inspection of the data indicates that rain-affected locations have winds that are often consistent with nearby locations where rain is not detected.

3. Mesoscale cyclogenesis from TCS-025

3.1. *Overview of period 29 August to 03 September*

There are two cyclones of interest that arose from the remnants of TCS-025, denoted C1 and C2, depicted in the evolution of vorticity at 850 hPa in Fig. 1. The NRL P-3 and Air Force C-130J aircraft observed TCS-025 on 27 and 28 August (Raymond et al., 2011). TCS-025 was classified as a non-developing depression that formed on the flank of a tropical upper tropospheric trough (TUTT) cell.

On 29 August, TCS-025 is clearly identifiable as a complex region of cyclonic vorticity equatorward of 25°N (Fig. 1a). Horizontal deformation acts to strain the

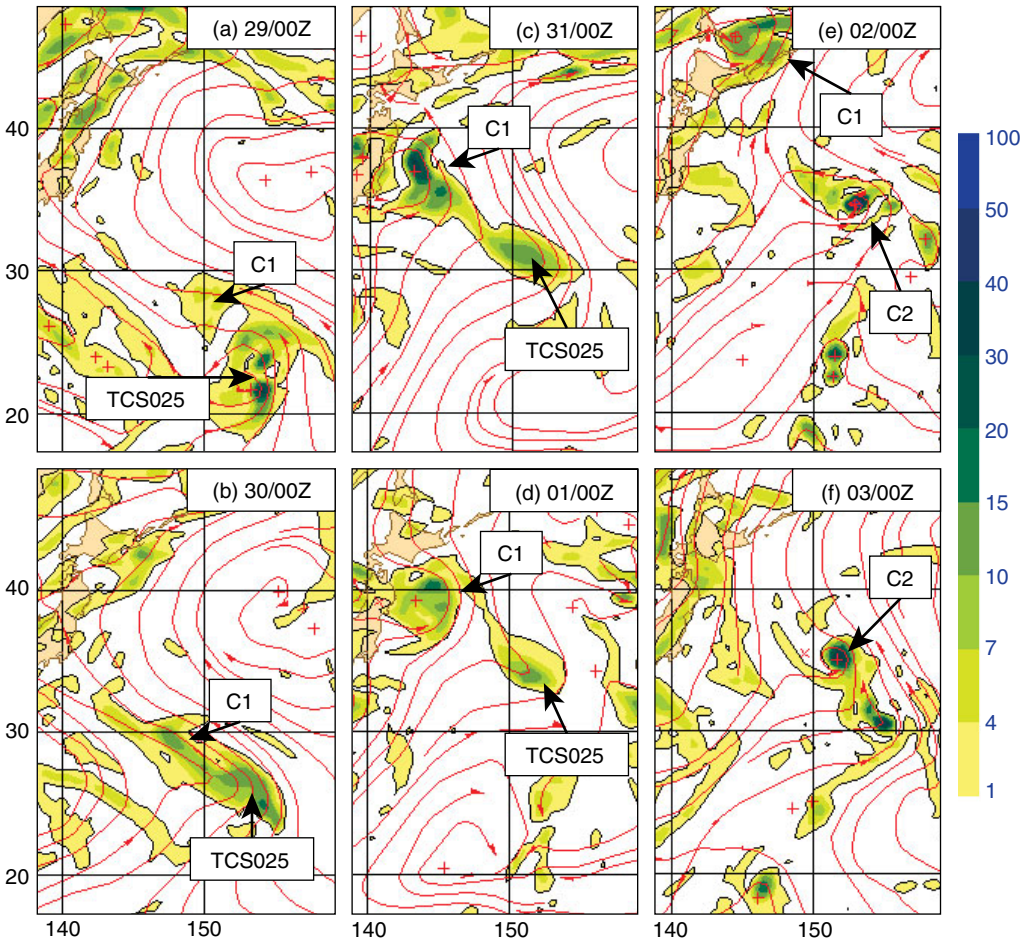

Fig. 1. Relative vorticity (yellow and green) and streamlines (red) at 850 hPa from ECMWF analyses. Cyclones C1, C2 and the remnants of TCS-025 area labelled.

vorticity along a northwest–southeast axis and is at least partly responsible for the lack of intensification of TCS-025 prior to 30 August. This deformation and the related strong southeasterly flow result from the juxtaposition of a cyclonic gyre to the west of TCS-025 and the anticyclone to the northeast. By 00 UTC 30 August, two centres of vorticity are evident (and may have been distinct even 24 h earlier). The centre that intensifies into C1 is located near 30°N, 148°E. Vorticity evolution in the ECMWF analyses points to the rapid consolidation and intensification of C1 late on 30 August (Fig. 1b, c). As this feature moves rapidly northwestward to a position near the coast of Japan on 31 August, the maximum vorticity increases and the elongation of the vorticity field becomes less pronounced.

The remainder of the vorticity complex that defines TCS-025 drifts northward from 29 August to 1 September (Fig. 1a–d) whereupon it suddenly re-intensifies late on 1 September. The lower-tropospheric vorticity maximum that defines C2 remains roughly stationary on 2 and 3 September, after which it weakens.

The period 29 August to 3 September, 2008, is characterized by a large-amplitude ridge in the upper troposphere, the filamentation of a significant trough and the separation of two distinct patches of PV from this trough (Fig. 2). These patches each become upper-tropospheric cold lows much like what were identified by Riehl (1948) and Sadler (1976) as TUTT cells. Cyclone C1 is influenced by a cold low that is connected to a synoptic-scale trough by a filament of low-potential temperature air on the dynamic tropopause on 31 August, analogous to a ribbon of enhanced PV on an isentropic surface. A second filament is extruded from the trough on 1 September (Fig. 2c, d) and influences the development of C2. The sudden appearance of localized, high-potential-temperature air on the edge of the trough suggests that diabatic processes may be eroding the trough at this time (0000 UTC 2 September, Fig. 2d). This time also represents the period of maximum intensification of C2. By contrast, C1 has weakened to the point that it is barely noticeable to the north of Japan.

Consistent with the presence of upper-tropospheric disturbances is moderate wind shear throughout the troposphere. In Fig. 3, this is summarized as the shear from 850 to 500 hPa, expressed as the magnitude of the vector wind difference. The winds associated with the vorticity and divergence within 4° (latitude) of the storm centre have been removed following the method of Davis et al. (2008),

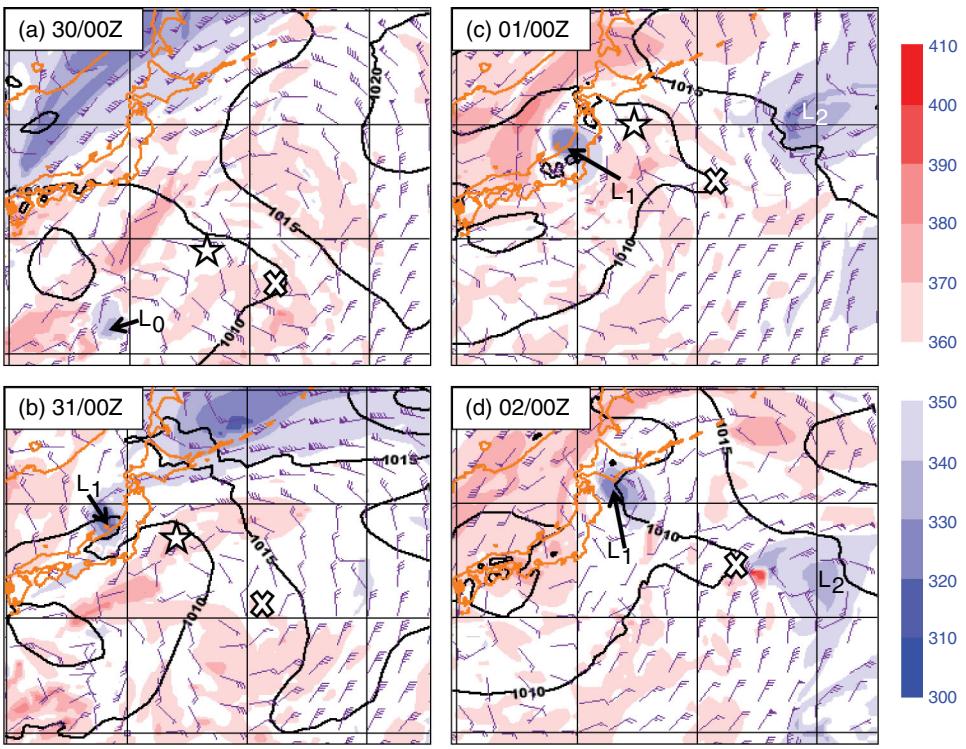

Fig. 2. Maps of potential temperature (K) and wind on the 2 PVU surface of potential vorticity (1 PVU = 10^6 m^2K $kg^{-1}s^{-1}$) valid along with contours of sea-level pressure (5 hPa interval) at 00 UTC on: (a) 30 August, 2008; (b) 31 August; (c) 1 September; and (d) 2 September. Star symbols indicate cyclone C1 and X symbols indicate C2 (remnant of TCS-025). 'L' symbols indicate cold lows on the tropopause, with L_1 and L_2 associated with C_1 and C_2, respectively.

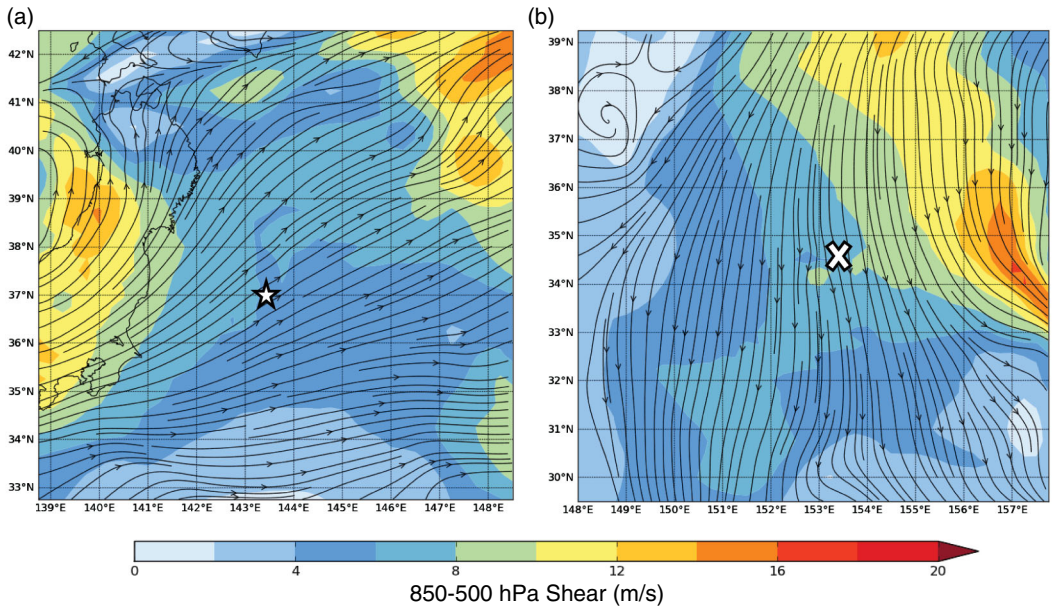

Fig. 3. Vector shear, depicted as streamlines and shear magnitude (m/s), in the layer from 850 to 500 hPa from the ECMWF analysis valid 00 UTC: (a) 31 August; and (b) 2 September. Disturbance has been removed prior to shear computation. Location of C1 is indicated by the star, and C2 is indicated by the white 'X'.

where the centre is defined as the location of maximum vorticity at 850 hPa, also averaged within a 4° radius. The two times shown, 0000 UTC 31 August and 0000 UTC 2 September, represent times when intensification is occurring. In both cases, the wind shear is about 7 ms^{-1} in the vicinity of the lower-tropospheric cyclonic circulation centre. The direction of the shear is maintained through the troposphere, and the shear reaches a magnitude greater than 10 ms^{-1} for C1 and 18 ms^{-1} for C2 (not shown) when averaged from 850 to 200 hPa.

The area where C1 develops marks the transition to cooler ocean surface temperature (Fig. 4). The sea-surface temperature beneath the intensifying cyclone C1 decreases from about 28°C near 30°N at 0000 UTC 30 August to less than 26°C near 37°N at 0000 UTC 31 August. The underlying SST in the region where C2 develops is relatively uniform near 28°C. The baroclinicity at the surface is partially reflected at 850 hPa, especially to the west of 160E (Fig. 4b, c). The general southerly or southeasterly flow direction results in warm advection and implied gradual lifting over a broad region east of Japan. Both C1 and C2 develop on the warm side of regions of weak baroclinicity (Fig. 4b, d)

Regarding the moisture distribution, relative humidity at 850 hPa reveals a large region near saturation in association with TCS-025 on 29 August (Fig. 5a). A well-defined plume of moisture develops as southeasterlies strengthen at 850 hPa (Fig. 5a) and air with high moisture content moves rapidly northwestward on 30 August. A greatly expanded region of near- saturated conditions accompanies the development of C1 late on 30 August (Fig. 5b, c). Such an expansion of near-saturated conditions, together with the regional warm advection already alluded to, implies mesoscale lifting. By 1 September, dry air at 850 hPa is being wrapped around the cyclone centre (Fig. 5d). The development of C2 commences in a recently expanded region of near-saturated conditions (Fig. 5d), similar to the case for C1. High relative humidity associated with the development of C2 is ultimately more localized than for C1, but peak mixing ratios of water vapour are similar, nearly 16 g kg^{-1} at 850 hPa (not shown). In its mature state, dry air is also being wrapped around and apparently into the cyclone (Fig. 5f).

3.2. *Development processes in cyclones C1 and C2*

Scatterometer observations from QuikSCAT and ASCAT confirm that the formation of C1 begins with a surface wind maximum early on 30 August (Fig. 6a). This feature is associated with an extensive area of deep convection that is loosely organized along a northwest to southeast axis. At 1831 UTC on 30 August, there is a better-defined cyclonic curvature to the winds, and two circulations are suggested in Fig. 6b. The centre near the western edge of the plot (near 142°E) appears to be the primary circulation centre present in the ECMWF analysis by 0000 UTC 31 August (Fig. 1c). However, most of the deep convection is associated with the stronger cyclonic circulation along

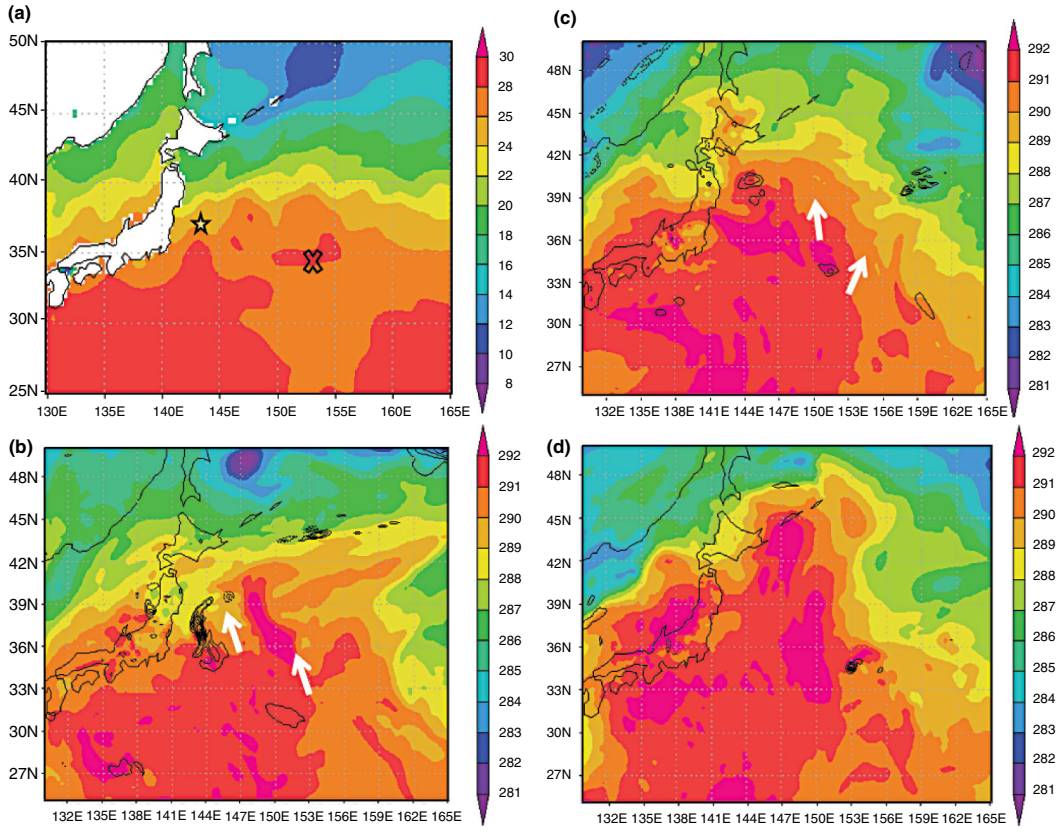

Fig. 4. (a) Sea-surface temperature analysis valid 00 UTC 31 August; (b) virtual temperature (shaded) and relative vorticity at 850 hPa valid 00 UTC 31 August; and (c) as in (b), but for 0000 UTC 1 September; and (d) as in (b) but for 0000 UTC 2 September. White arrows in (b) and (c) indicate the flow direction at 850 hPa as depicted in Fig. 1. The star and 'X' in panel (a) denote the locations of C1 at 0000 UTC 31 August and C2 at 0000 UTC 2 September, respectively.

145°E (Fig. 6e). Convection is located almost entirely to the north and east of the centre where the southeasterly surface winds are strongest.

The circulation featured in Fig. 6b actually becomes the dominant circulation feature by 0734 UTC 31 August (Fig. 6c). In conjunction with this feature, the cold cloud shield has further organized and now partially overlies the centre. The coldest cloud tops are located to the east of the surface circulation centre, again above strong surface southeasterlies. Animations reveal that the warm-cloud notch in the system along 146E is the signature of southerly flow that is likely to be transporting drier air northward, as was suggested in Fig. 5d.

Observations from the DLR Falcon near 0000 UTC 30 August depict the vertical structure of the plume of moisture streaming from the tropics into the subtropics (Fig. 7a). Dropsondes reveal high equivalent potential temperature, θ_e, in excess of 350 K up to 800 hPa (Fig. 7a) in the presence of southeasterly winds. Winds through a deep layer (950–500 hPa) feature weak vertical shear and average approximately 15 ms^{-1}. Given the relatively strong flow and weak shear at this time, the tropical plume of air would be expected to progress rapidly northwestward and roughly maintain its structure. As indicated by dropsonde 10, considerable conditional instability exists within this air mass (Fig. 7b) with convective available potential energy (CAPE) for undiluted parcels exceeding 1000 J kg^{-1}, and with little convective inhibition. As this air moves northwestward, isentropic upglide under even weakly baroclinic conditions would be sufficient to initiate widespread, deep convection. Such conditions are apparent during the following day.

Analysis of conditions near 00 UTC 31 August is augmented by another Falcon mission that captures the increasingly baroclinic nature of the flow and developing frontal structure associated with the circulation centre near the coast of Japan (Fig. 8). The dropsondes capture the lower-tropospheric easterly flow on the north side of the cyclone centre located near 37°N, 143°E. A comparison of winds at 850 and 500 hPa indicates that this region of the cyclone is strongly sheared, with southerlies or south-westerlies generally in the middle-troposphere associated

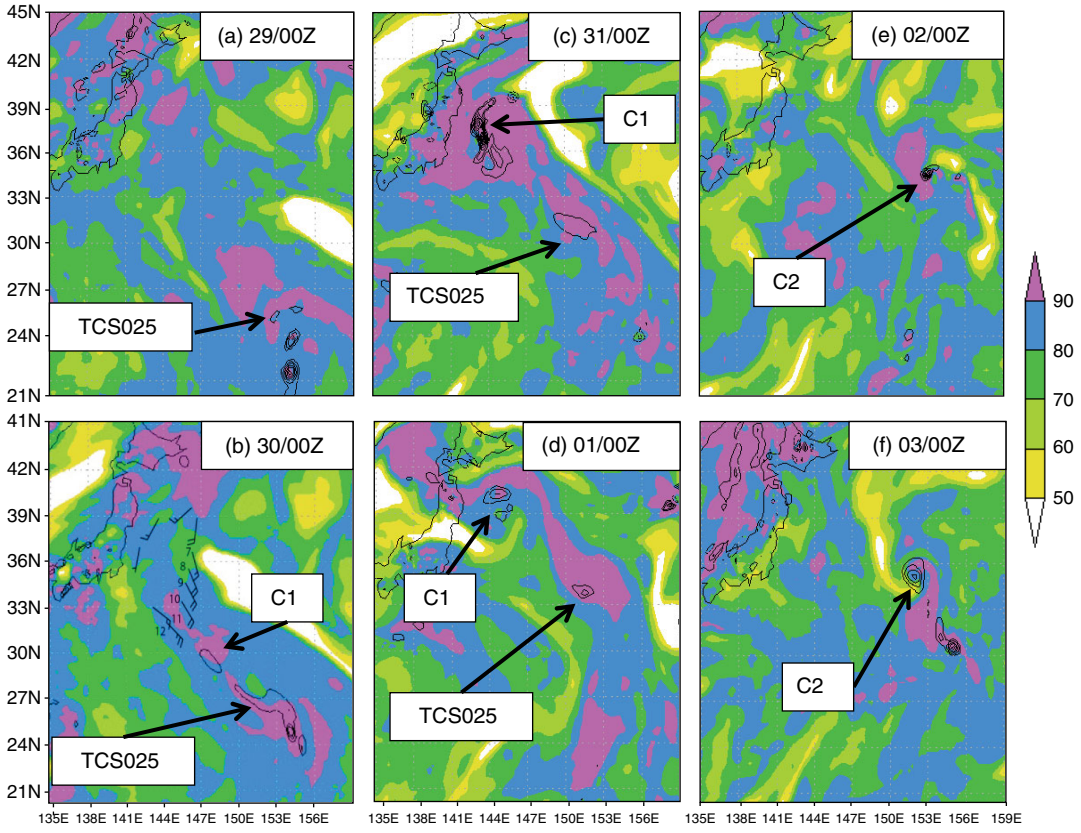

Fig. 5. Relative humidity and relative vorticity at 850 hPa at 0000 UTC daily from 29 August to 3 September in (a)–(f), respectively. Cyclones are labelled as in Fig. 1. Panel (b) shows dropsonde winds at 850 hPa and numbered soundings to appear in Fig. 7.

with the upper-tropospheric cold low over Japan at this time (Fig. 2b). The northeastward extension of high vorticity near 39°N 144°W and associated thermal contrast (Fig. 4b) are indicative of a warm front in the analysis. The presence of this frontal region is consistent with the dropsondes that reveal a wind profile veering with altitude. Furthermore, the expansive, moderately cold cloud shield poleward of this developing frontal feature is consistent with broad ascending motion. The developing warm-frontal feature also coincides with the gradient of sea-surface temperature (Fig. 4a) that exists along the north wall of the Kuroshio current. Tropical air moving over the cooler water results in nearly saturated and stable boundary layers within the easterly flow north of the front-like feature (not shown). At 850 hPa, the magnitude of the temperature gradient is roughly 1°C per 300 km.

The infrared image from 0030 UTC 31 August (Fig. 8), intermediate between the times shown in Fig. 6e and f, reveals convection becoming organized to the east of the primary cyclone centre in the analysis, and slightly poleward of the secondary vorticity maximum along 145°E. This secondary vorticity maximum may be poorly represented in the analysis, but its location is consistent with linear interpolation of the positions of circulation centres marked in Fig. 6b and c that were inferred from the scatterometer data. Based on the scatterometer, dropsonde and IR data, we conclude that cyclone C1 consists of two separate circulation centres. The centre to the northwest is well resolved in the ECMWF analyses and also appears to have baroclinic characteristics and developing frontal structure by 00 UTC 31 August. A second circulation centre develops late on 30 August and intensifies rapidly on 31 August in conjunction with a large mesoscale convective system. The second centre becomes the dominant circulation feature later on 31 August.

To further diagnose the development of C1, we rely on information derived from 12-h forecasts from the ECMWF model initialized at 12 UTC 30 August. While the ECMWF forecasts did not necessarily resolve all of the details in the development of C1, these forecasts did predict the rapid development of a mesoscale cyclone at approximately the correct time and location. The position of the forecast cyclone at 0000 UTC 31 August was actually between the two circulation centres identified above (see Fig. 9). The extensive output from the model, made available through the YOTC initiative (Waliser and Moncrieff, 2008), allows

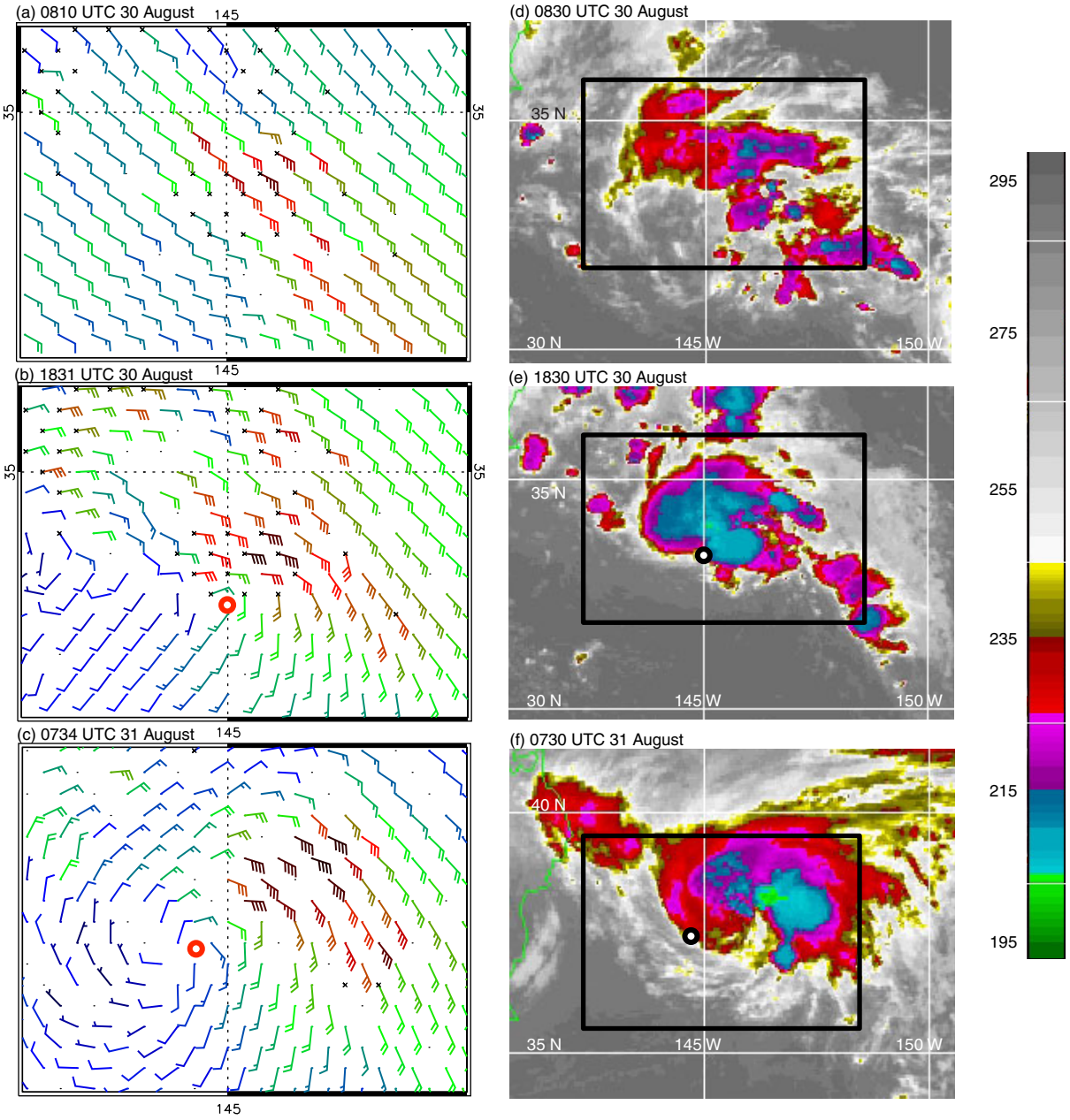

Fig. 6. QUIKSCAT-derived surface winds valid: (a) 0810 UTC August 30; (b) 1831 UTC August 30; and (c) 0734 UTC 31 August. Long barb is 5 m/s and barbs are coloured according to wind speed. Black dot with no wind plotted indicates wind failed variational quality control test (i.e. is spatially inconsistent); 'x' indicates rain detected. (d) IR image valid 0830 UTC 30 August; (e) IR image valid 1830 UTC August; and (f) IR image valid 0730 UTC 31 August. Black boxes in (d), (e) and (f) indicate areas shown in (a), (b) and (c), respectively. Red circles in (a)–(c) and black circles in (d)–(f) indicate the location of mesoscale cyclone centre.

diagnosis of physical processes that are informative about the cyclogenesis that was realized.

The developing cyclone at 0000 UTC 31 August is characterized by a narrow, upright maximum of potential vorticity that extends to about 400 hPa (Fig. 9a, b). From Fig. 9a, it is apparent that the vortex tilts slightly northeastward with height. The mid-tropospheric PV feature over the southern part of the domain can be traced directly back to TCS-025, but it does not appear to be significant in the formation of C1.

The process of surface cyclone intensification is now examined with the aid of a vorticity budget in a

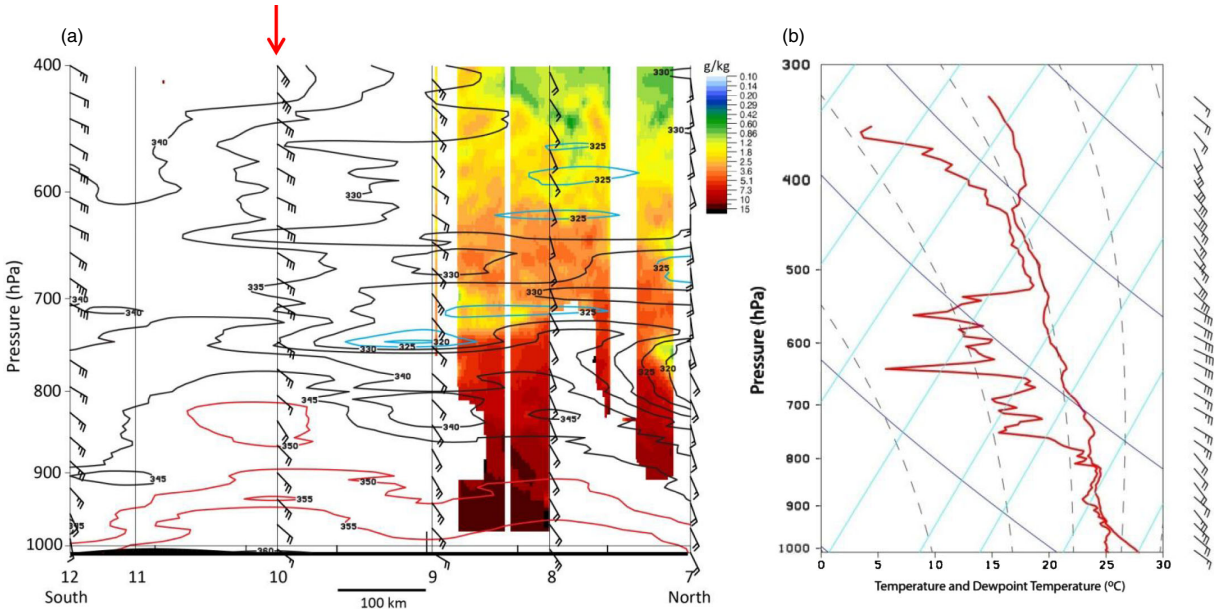

Fig. 7. (a) cross section (soundings 7–12 in Fig. 5b) of equivalent potential temperature (5 K contour interval), wind and water vapour mixing ratio from DIAL aboard the DLR Falcon (g/kg) valid at approximately 00 UTC 30 August; (b) skew-*t* depiction of sounding 10, located by red arrow in panel (b).

system-following frame of reference (Sec. 2).[3] To evaluate the accuracy of the budget, we compare the accumulated 12-h changes estimated from the full right-hand-side of the vorticity equation with the actual changes in area-averaged vorticity in the forecast (Fig. 10a). The averaging area is a box that is 5° on a side (Fig. 9a). The area-average vorticity changes represent the mean of an 81-member ensemble budget in which the location of the box is varied from its average position in order to assess the sensitivity of the various budget terms. This sensitivity is summarized by profiles of the *t*-statistic, $t_i = \frac{\zeta_{t_i}}{\sigma/\sqrt{N}}$, where ζ_{t_i} refers to the *i*th vorticity tendency term, σ is the sample standard deviation and N represents the number of degrees of freedom[4] (Fig. 10b). The basic vertical profile is captured from the right hand side terms, but there is an offset in which the change in vorticity is less than the estimated change. One source of error is the relatively coarse time interval of model output that may render invalid the assumption that changes are linear in time.

The stretching term clearly dominates the vorticity budget (Fig. 10a) and largely accounts for the positive tendency of area-mean cyclonic vorticity in the lower troposphere, and negative vorticity tendency in the upper

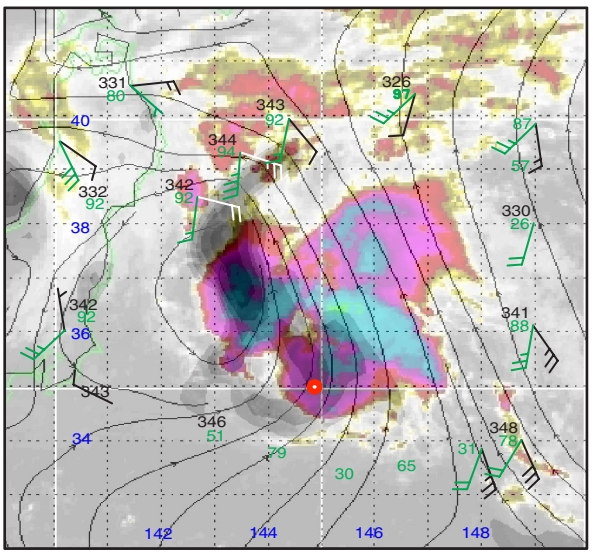

Fig. 8. Equivalent potential temperature and wind at 850 hPa (black or white wind barbs), relative humidity and wind at 500 hPa (green) superposed on ECMWF vorticity analysis (grey) at 850 hPa, valid 00 UTC 31 August and IR satellite image valid 0030 UTC 31 August (colour). Colour scale as in Fig. 6. Red circle indicates the estimated location of the developing mesoscale cyclone at 0000 UTC based on positions indicated in Fig. 6.

[3]The positions of the box every 3 h during the first 12 h of the forecast are: 32.0°N, 145.0°E; 33.0°N, 144.75°E; 34.25°N, 144.50°E; 35.50°N, 144.25°E; and 36.5°N, 144.0°E.

[4]Ordinarily, N is the size of a randomly chosen sample, but in the present case, the sample has not been chosen randomly and therefore the effective sample size, representing the degrees of freedom, is considerably less than the full ensemble size. We have assumed $N = 9$ to account for this in computing the *t*-statistic. Choosing N with a value as small as 4 still maintains the significance of the stretching term near the top and bottom of the analysis domain and friction in the lower troposphere.

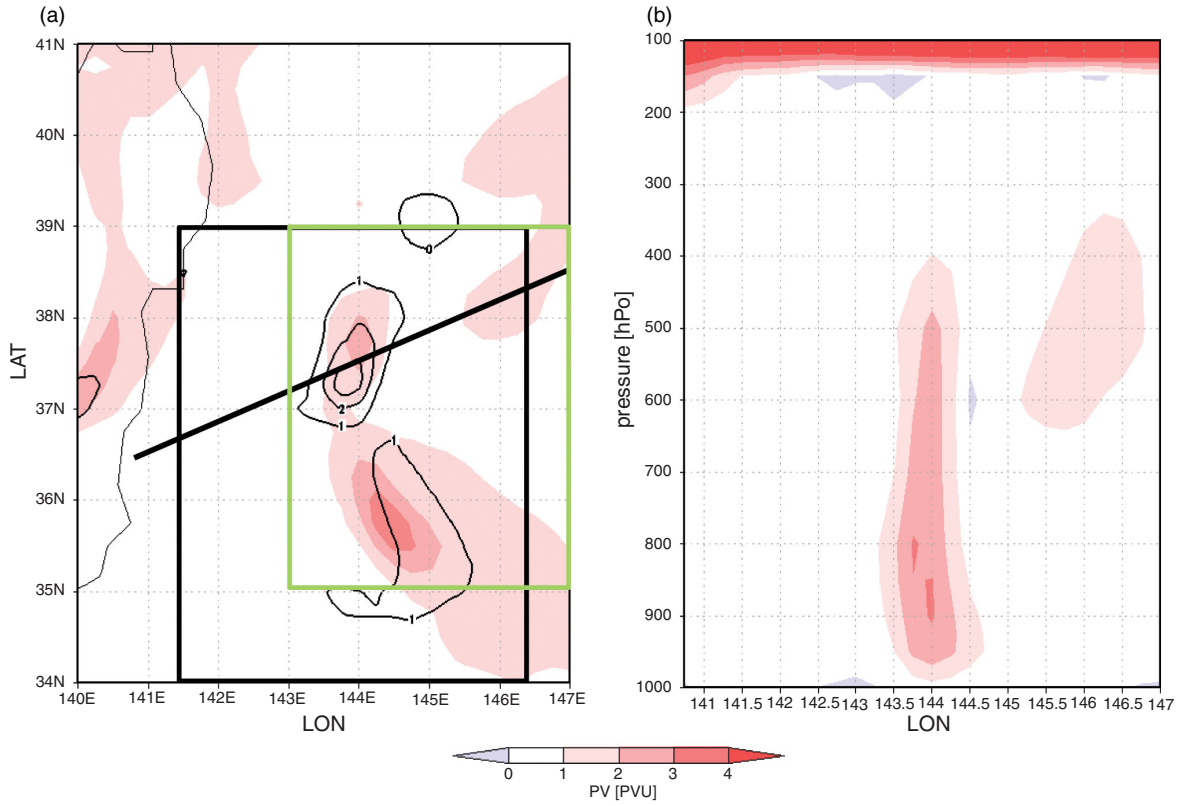

Fig. 9. (a) Potential vorticity at 850 hPa (contours) and 500 hPa (colours) from ECMWF forecast initialized at 12 UTC 30 August valid 00 UTC 31 August; (b) cross section of PV along segment shown in (a) directed approximately along the direction of vertical shear. Contour interval in (a) is 1 potential vorticity unit (PVU), with 1 PVU $= 10^{-6}$ m^{2}K kg^{-1}s^{-1}.

troposphere associated with divergence. Furthermore, the stretching tendency is considerably larger than the apparent imbalance in the budget. Vortex stretching redistributes an initially relative uniform profile of box-averaged vorticity (not shown) into a concentrated positive anomaly in the lower troposphere and negative relative vorticity aloft. The increase of vorticity is greatest near the top of the boundary layer, which is also effectively the cloud base. There is no evidence that lower-tropospheric divergence, which would occur from convective downdrafts, limits the increase of vorticity. The low value of the *t*-statistic for the eddy-flux term indicates that its value is highly sensitive to the exact placement of the box (Fig. 10b). The frictional tendency is not particularly sensitive and, perhaps surprisingly, there is a tilting signature in the middle troposphere that is relatively robust.

Now considering the development of C2 on 1–2 September, recall that the vorticity associated with TCS-025 was elongated northwest to southeast in a deformation flow, and that the eastern portion of the vorticity drifted northward beginning on August 30 (Fig. 1). Convection associated with this feature remains minimal until 00 UTC 1 September when the lower-tropospheric cyclonic vorticity approaches the upper-tropospheric cold low (Fig. 2c). By late on 1 September, deep convection becomes organized slightly to the south of the axis of maximum horizontal shear inferred from the ASCAT observations (Fig. 11a, c). The southward displacement of convection arises because the troposphere in this region is characterized by northerly vertical wind shear (Fig. 3b). The wind field quickly attains a cyclonic curvature that is well observed by ASCAT at 1034 UTC 2 September (Fig. 11b). By this time, convection has weakened considerably (Fig. 11d) and occurs mainly above the surface convergence or trough line that extends southward from the cyclonic circulation centre. Although new bursts of convection do occur near and downshear from the cyclone centre later on 2 September, none is sustained. The circulation increase apparent in Fig. 11 is primarily the result of a single mesoscale convective burst.

The intensification of C2 is captured well in the ECMWF forecast initialized at 1200 UTC 1 September, which reveals a narrow, deep column of enhanced potential vorticity (Fig. 12a, b) at 0000 UTC 2 September. The east–west elongation in the potential vorticity at 850 hPa that was seen in the scatterometer data is also well defined to the west of the maximum vorticity in the analysis. The vortex

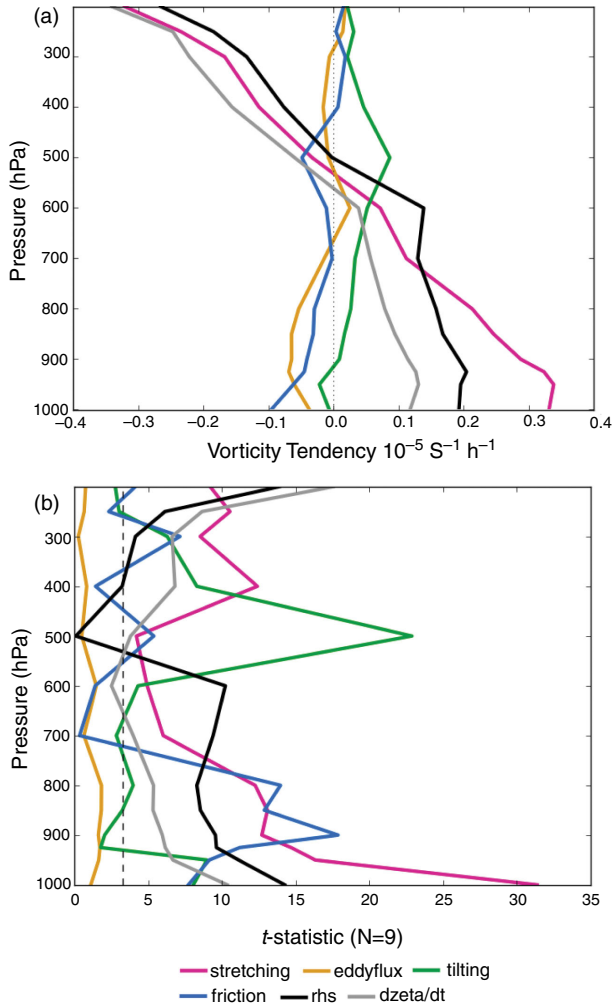

Fig. 10. (a) Vorticity changes from 1200 UTC 30 August to 0000 UTC 31 August, representing the mean of the 81-member ensemble budget; and (b) *t*-statistic for each profile in (a); dashed line is 99% confidence value.

tilts slightly southward with height (Fig. 12a, b), and this direction is consistent with the analysed vertical shear at this time (Fig. 3b). The PV column features maxima from 800 to 900 hPa and also at 500 hPa. The mid-tropospheric vorticity and potential vorticity maximum is greater in C2 than in C1. The vorticity budget for C2 (not shown) also indicates strong stretching maximized in the boundary layer as for C1, as well as larger contributions of a positive eddy flux of vorticity associated with the proximate upper-tropospheric cyclonic vortex and a cyclonic tendency near 300 hPa due to vortex tilting, all of which result in a deeper cyclonic vortex in C2.

From the column of enhanced PV and the vorticity budgets in both C1 and C2, we can infer the importance of condensation heating in the production of strong vertical motions and vortex stretching in the lower troposphere. The diabatic processes are now further quantified by computing profiles of temperature and water vapour mixing ratio tendencies from the ECMWF model, partitioned according to various physical processes (Fig. 13). Averaged over a 4-degree box (green box in Fig. 9a[5]), the profile for C1 reveals strong heating due to the cumulus scheme, with a maximum near 600 hPa. The grid-scale precipitation scheme produces slight cooling in the boundary layer, and a maximum of heating near 400 hPa. Combined, these produce diabatic heating that increases monotonically upward through 500 hPa. The dynamics term is dominated by vertical advection and adiabatic cooling up to at least 500 hPa. The deep diabatic heating, increasing up to approximately 400 hPa, is consistent with the depth of the PV column (Fig. 9c) and the depth of the positive vorticity tendency due to stretching (Fig. 10a) is consistent with the depth of the inferred mean ascent.

In the boundary layer, turbulent fluxes offset the cooling due to microphysical processes, resulting in little net change of temperature. There is a net moistening in the boundary layer, but more impressive moistening above the boundary layer (the top of the boundary layer lies where the turbulent flux becomes small, or about 950 hPa). The net moistening of the lower troposphere is the result of microphysical processes (mainly evaporation, consistent with the cooling in the lowest 2 km), fluxes from the ocean and vertical transport. The dynamics term does not distinguish between locally induced transport in convective motions and the regional moisture transport inferred from Figs. 4 and 5. Indeed, both are probably occurring. The tendency for moistening is partially countered in the lower troposphere where condensate is removed by the convection scheme.

Area-averaged profiles of temperature and moisture changes for C2 (Fig. 13b, d) indicate some similarities with the convection that occurs during the formation of C1. The diabatic heating is quantitatively similar, with peak heating values and the pressure at which they occur being nearly identical to the profiles for C1. Furthermore, there is also weak cooling in the boundary layer produced by the grid-scale condensation scheme.

However, the moisture changes from 21 UTC 1 September to 00 UTC 2 September differ somewhat from C1. In particular, the dynamics contribute a strong negative moisture tendency in the present case, whereas it was strongly positive for C1. The negative moisture tendency occurs over an even deeper layer at 0600 UTC

[5]The location and size of this box differs slightly from the box used in the vorticity budget in order to capture the full extent of the precipitating region in the model. Furthermore, the box does not move in the computation of tendencies of temperature and water vapour shown in Fig. 13.

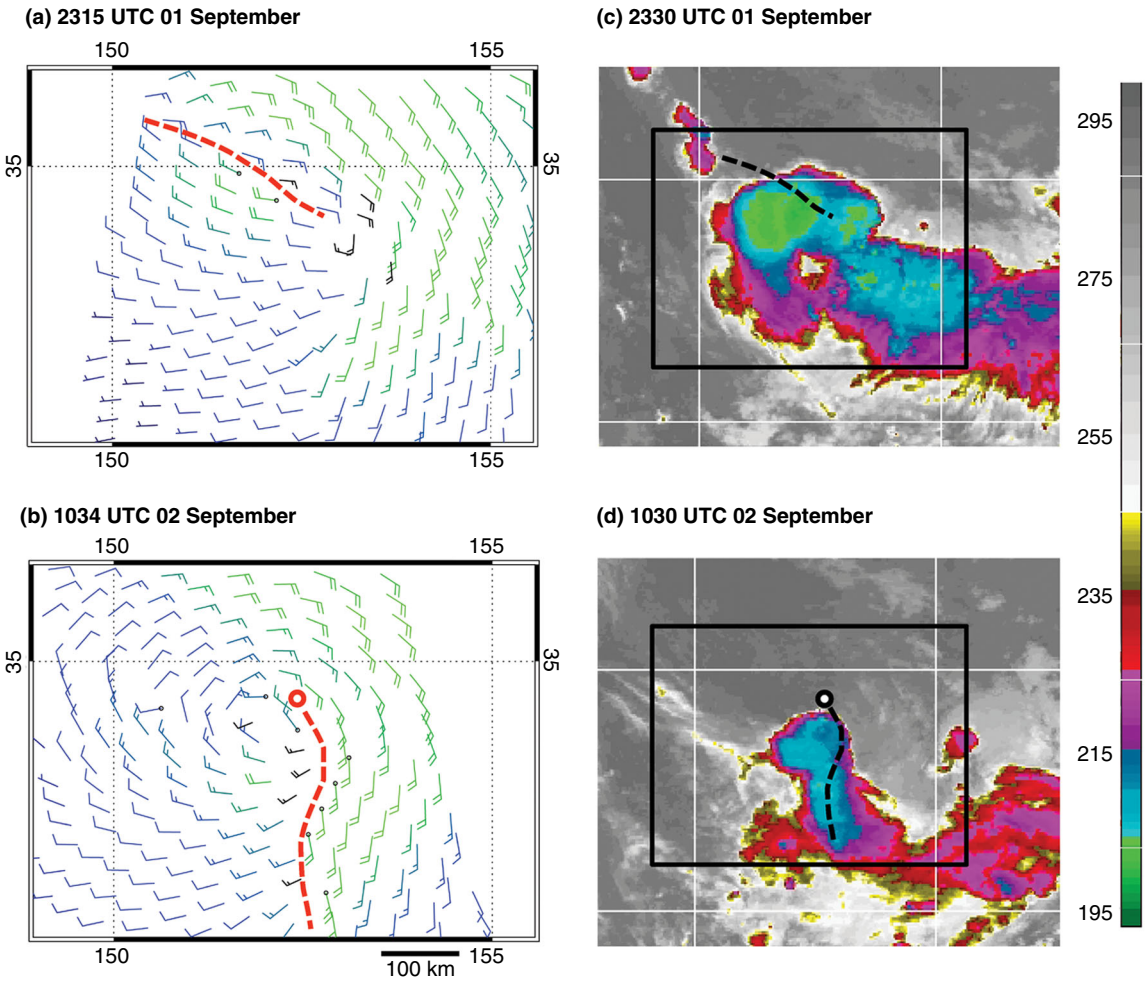

Fig. 11. Advanced Scatterometer (ASCAT) surface winds valid: (a) 2315 UTC 01 September; and (b) 1034 UTC 02 September; (c) IR satellite image for 2330 UTC 01 September; and (d) IR image for 1030 UTC 02 September. Black dot indicates wind failed variational quality control test (i.e. is spatially inconsistent); 'x' indicates rain detected. Black boxes in (c) and (d) indicate areas shown in (a) and (b), respectively. Heavy dashed lines indicate wind shift lines. Red and black circles in 9b) and (d), respectively, indicate cyclone centre location.

2 September (not shown). This indicates the importance of horizontal moisture advection in C2. Recall the proximity of dry air in the lower troposphere near the cyclone centre (Fig. 5e, f). Horizontal transport of dry air into the box can also be inferred from the spatial pattern of relative humidity in Fig. 5f at 0000 UTC 3 September. From Fig. 5f, it appears that the dry air actually penetrates the high vorticity core of C2 and probably explains why there was only a single burst of convection coincident with the high vorticity region.

From the standpoint of potentially developing a tropical cyclone, the environments of C1 and C2 are clearly hostile because of the presence of rather strong vertical wind shear and dry air, especially in the case of C2. Nonetheless, the shear is what helps initiate the convection that intensifies the vortical remnants of TCS-025. The existence of significant vorticity in the boundary layer prior to when convection organizes is also an important factor for intensifying the surface circulation. In C1, the tropical moisture plume is responsible for initiating deep convection that organizes upscale and, despite a relatively short period conducive to development (roughly 24 h), produces a surface cyclone with winds of tropical cyclone strength. With time, however, in each case the thermodynamic environment becomes hostile for sustaining the deep convection that might have built a stronger cyclone. Cyclone C1 is affected by the traversal of the system over cooler water which stifles the development of further deep convection and by its encounter with strong vertical shear and horizontal deformation near 40°N. In C2, dry air

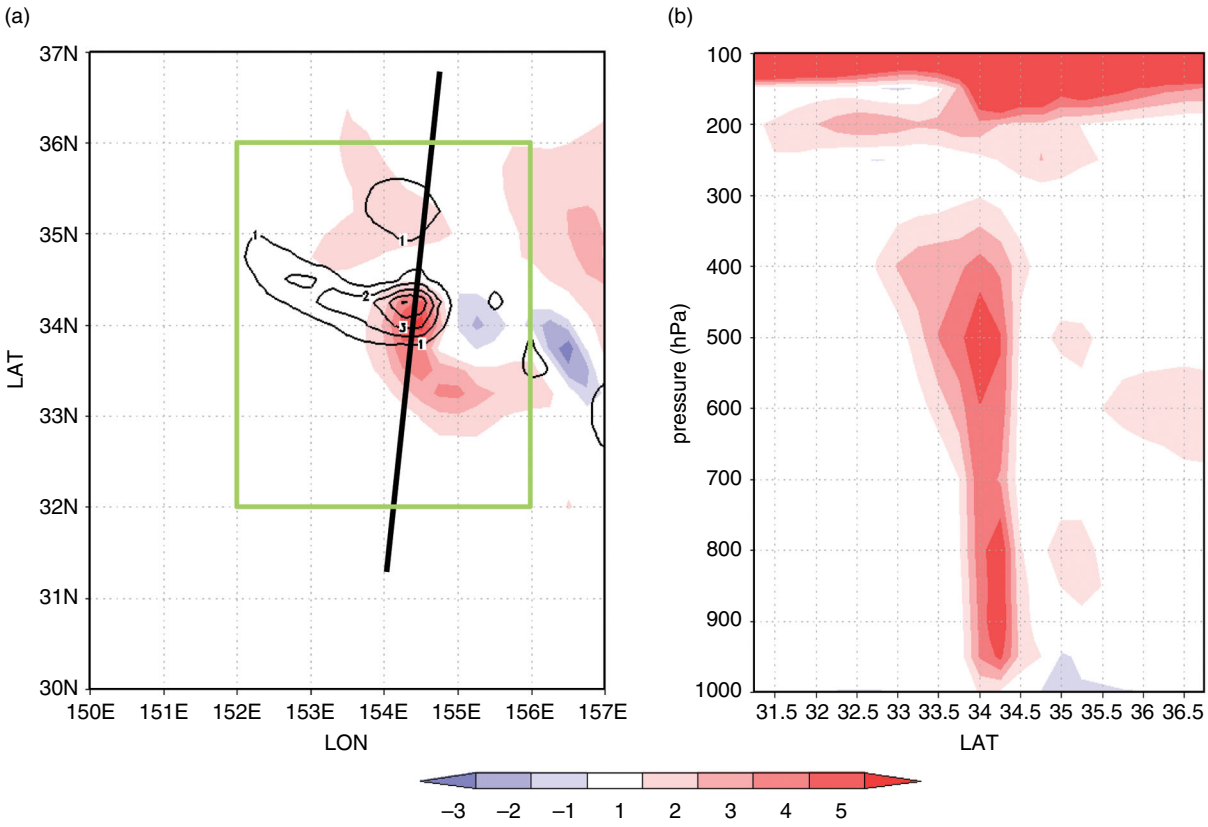

Fig. 12. (a) Potential vorticity at 850 hPa (contours) and 500 hPa (colour) from ECMWF forecast initialized at 12 UTC 01 September valid 00 UTC 02 September; (b) cross section of PV along segment shown in (a) directed approximately along the direction of vortex tilt. Contour interval in (a) is 1 potential vorticity unit (PVU), with 1 PVU $= 10^{-6}$ m^{2}K kg^{-1}s^{-1}.

continues to invade the lower-troposphere around the cyclone, limiting the potential for deep convection, and vertical shear promotes decay of the vortex.

4. TCS-037: Development of a TC in the subtropics

The early stages of TCS-037 were examined in Raymond et al. (2011) centred on 0000 UTC 8 September. The disturbance featured strong cyclonic circulation, especially in the middle troposphere, and was embedded in an environment of relatively weak vertical wind shear. Strong horizontal gradients of specific humidity were present and indicated considerable dry air near the centre of circulation in the co-moving frame of reference. This dry air was considered to inhibit the development of TCS-037 prior to September 9.

The representation in the ECMWF analyses of TCS-037 appears in Fig. 14. At 00 UTC 8 September, the centre of circulation was determined by Raymond et al., to lie at 26°N 154°E, which is in close agreement with the ECMWF analysed maximum vorticity in Fig. 14a. Following this time, the disturbance moves west–northwestward and maintains a weak circulation at 850 hPa (Fig. 14b) and at the surface (Fig. 15a). Also apparent in Fig. 14b is the existence of a predecessor cyclone to the east of Japan on 8 September. This baroclinic cyclone is accompanied by a trailing cold front that is indicated by the north–south strip of vorticity in Fig. 14b that lay to the northwest of TCS-037. The remnant of TCS-037 intensifies later on 9 September, becoming TC 16W at 0000 UTC 10 September according to JTWC. The surface winds associated with this cyclone at 1107 UTC are seen in Fig. 15b. These winds exhibit a northeast-to-southwest elongation that suggests 16W might be influenced by vertical wind shear at this time (see also Fig. 18b).

Later on 10 September, the minimal TC turns northward and later northeastward as it passes along the east coast of Japan, subjecting that area to heavy rainfall (Fig. 14e, see also Fig. 16f). A transition to extratropical structure occurs on 11 September and the circulation is swept into a larger developing baroclinic cyclone on 13 September (Fig. 14f).

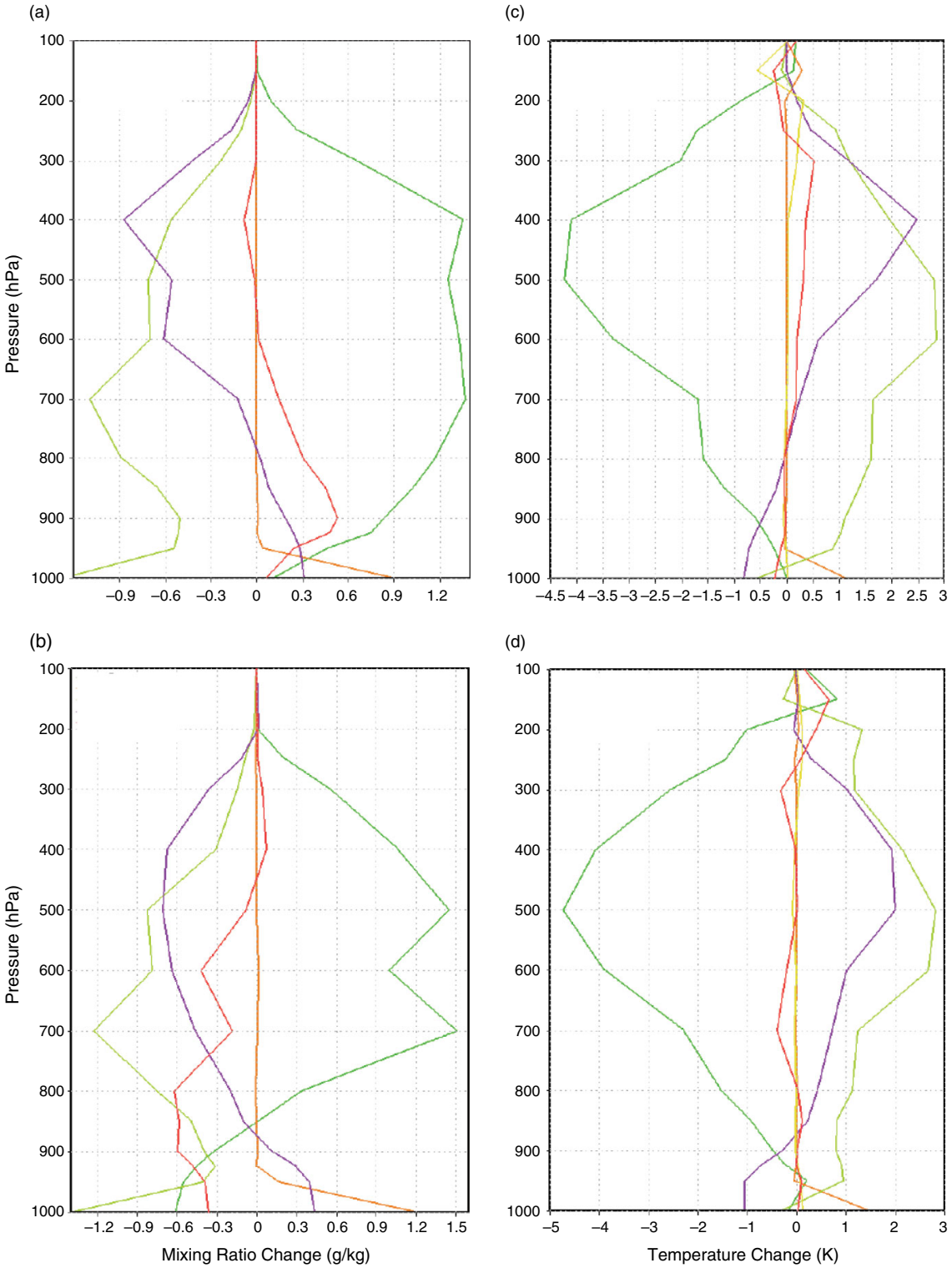

Fig. 13. Change in (a) water vapour mixing ratio (g/kg) averaged over green box in Fig. 9a from 2100 UTC 30 to 0000 UTC 31 August; (b) water vapour mixing ratio (g/kg) averaged over green box in Fig. 12a from 2100 UTC 01 to 0000 UTC 02 September; (c) and (d), as in (a) and (b), respectively, but for temperature changes (K). Green: dynamics (vertical and horizontal advection); purple: grid-scale cloud scheme; light green: cumulus scheme; orange: turbulent diffusion and fluxes; yellow: radiation (generally a small contribution); red: total change.

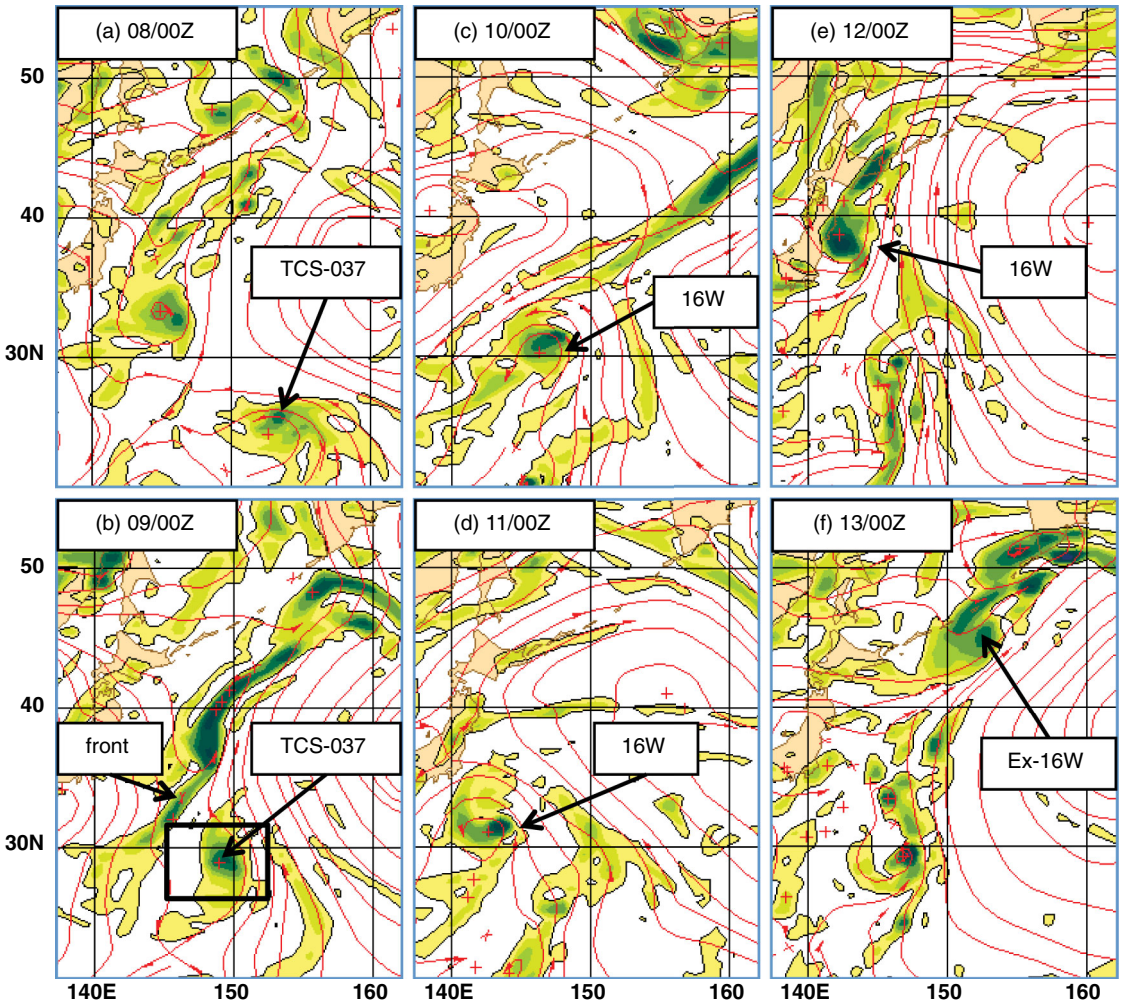

Fig. 14. Vorticity and streamlines at 850 hPa for TCS-037 (16W). Black rectangle in (b) is area shown in Fig. 15a.

Maximum surface winds reach 35 knots at 0000 UTC 10 September, but based on the ECMWF analysis, further strengthening of the overall cyclonic circulation continues into 11 September.

As TCS-037 approaches the cold front early on 9 September, the latter appearing as a separate, elongated cloud feature in Fig. 16a, deep and sustained moist convection develops over the cyclone centre (Fig. 16b, c). By 1957 UTC 9 September, deep convection associated with the front becomes no longer distinguishable from deep convection associated with TCS-037. The consolidated, convective burst (Fig. 16c) leads to a strong, curved rainband, apparent in TRMM imagery at 2103 UTC. By later on 10 September, convection is organized similarly to the classic 'Delta-rain-region' (Klein et al., 2000) as extratropical transition commences. Note that the scale of this rain region, as indicated by the ice-scattering signature of 85 GHz SSMI observations, is only about 200 km. By 0956 UTC 11 September (Fig. 16f), extratropical transition is nearly complete, and the cyclone is characterized by heavy rainfall to the northwest of the circulation centre.

A DLR-Falcon mission centred near 0000 UTC 09 September reveals some important mesoscale aspects of the flow prior to the development of 16W. The aircraft made two transects of the cold front (Fig. 17a), and each revealed a local maximum of equivalent potential temperature near the leading edge of the front with values near 345 K at 850 hPa. Equivalent potential temperature to the northwest of the front rapidly decreases primarily due to dry air. The actual virtual temperature change behind the front is about 2°C (Fig. 17b). The clear region between TCS-037 and the front exhibits slight lower θ_e values, especially along the southern flight leg returning toward Japan. Values of θ_e near the centre of TCS-037 are similar to the highest values associated with the front. Assuming

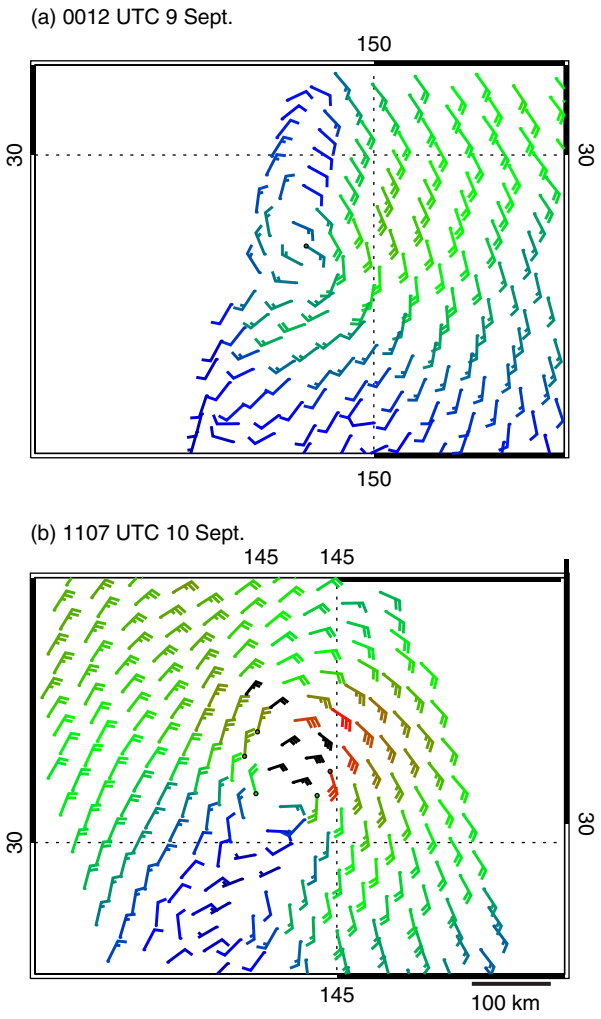

Fig. 15. ASCAT images for TCS-037: (a) 0012 UTC 9 September; and (b) 1107 UTC 10 September.

that the regions of enhanced θ_e are maintained for the next 18 h, the merger of TCS-037 with the front would result in an expanded region of high θ_e and, because most of the enhancement of θ_e is due to greater water vapour content, an expanded region of high relative humidity in the lower troposphere.

Also apparent in Fig. 17b is an area of relatively weak vertical wind shear to the southeast of the front. This is further quantified from the ECMWF analyses by removing the analysed disturbance and calculating the shear between 850 and 200 hPa (Fig. 18). At 1200 UTC 9 September, the remnant of TCS-037 is located in a region of weak vertical shear. The localized weak shear results from a favourable spatial relationship between multiple upper-tropospheric PV anomalies including the remnant TUTT cell that was observed to accompany TCS-037 (Raymond et al., 2011), a southwesterly jet to the northwest of the disturbance, and thermal ridges[6] to the southwest and northeast (Fig. 18a). A similar mechanism of shear reduction has been observed in other tropical cyclone developments (R. McTaggart-Cowan et al., 2008, personal communication). By 1200 UTC 10 September, TC 16W enters a region of increasingly strong southwesterly wind shear (Fig. 18b). Not surprisingly, this time coincides with the appearance of a delta rain region poleward of the circulation centre, and the beginning of extratropical transition.

5. Summary

The present study has examined the formation of three mesoscale cyclones in the subtropical region of the western Pacific Ocean during late August and early September of 2008 when the TPARC/TCS-08 experiment was taking place. Each of these cyclones could be traced back to a remnant tropical disturbance that did not achieve tropical cyclone status in the tropics. From these tropical remnants of vorticity and enhanced water vapour content, mesoscale cyclones rapidly intensified near or poleward of 30°N. Each cyclone was characterized by a primary burst of mesoscale convection (on scales of 200–400 km), and each notably intensified the pre-existing mesoscale surface vorticity as a result of this burst. Furthermore, the vorticity was initially elongated, especially in the cyclones of 31 August and 2 September, but rapidly evolved into a quasi-circular swirling wind field.

The first cyclone, termed C1, developed tropical storm-force winds on August 31, but was not classified as a tropical cyclone. The second storm, C2, was somewhat weaker than C1 and likewise not classified as a tropical system. The third storm achieved tropical cyclone status, 16W, on 9 September and produced a significant wind and rain event for eastern Japan on 11 September. Cyclones C1 and C2 are best classified as subtropical cyclones based on the importance of vertical shear and deep convection (organized by shear, Davis, 2010), and the development of attendant sub-cyclone scale shear lines evident in the surface wind field that represent the first signatures of fronts.

In each case, the primary burst of convection was organized as the moisture-laden, high-vorticity remnant of a tropical disturbance encountered mesoscale lifting of air in conjunction with a baroclinic feature. In the cases of C1 and C2, the feature was an upper-tropospheric cyclonic PV anomaly with deep (albeit weak) tropospheric baroclinicity

[6]The term 'thermal ridge' is an anticyclone in the vector shear field, which should be balanced by a localized positive anomaly of virtual temperature assuming that thermal wind balance, or gradient thermal wind balance, holds.

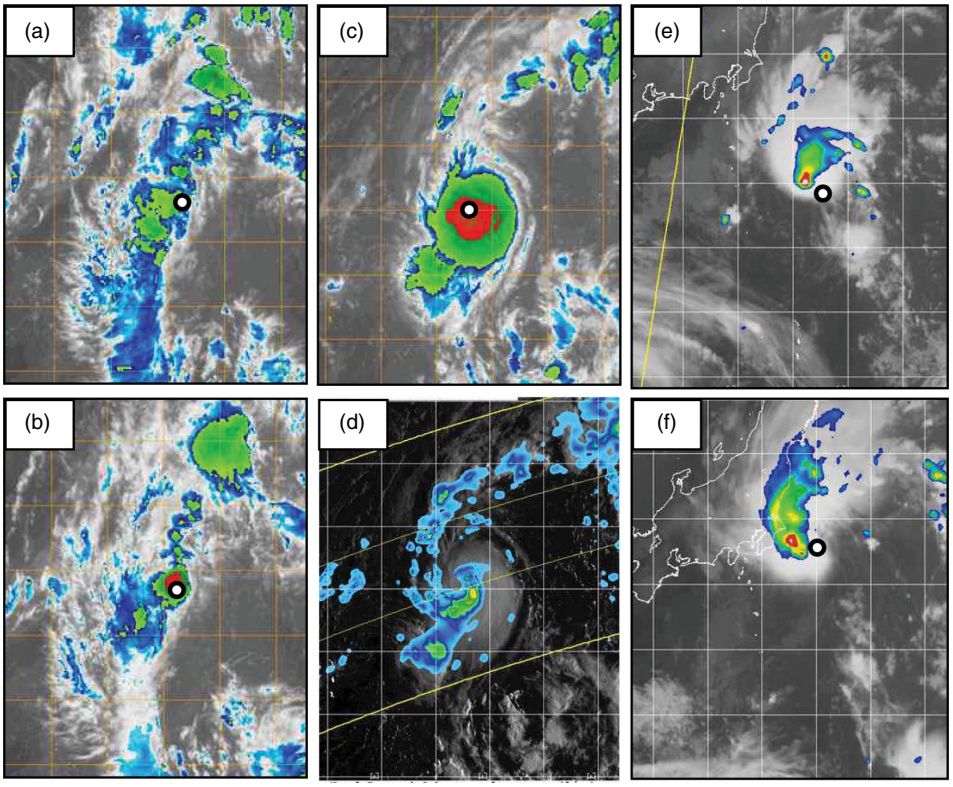

Fig. 16. (a)–(c) Infra-red cloud-top temperature at 0357, 0657 and 1957 UTC 9 Sept., respectively; (d) TRMM precipitation radar at 2103 UTC 9 September; (e) and (f) 85 GHz polarized corrected temperatures from SSMI at 10 September 2001, and 0956 UTC 11 September, respectively. White circle denotes centre of TCS-037.

accompanying this feature. In C1 and C2, there was flow in the lower troposphere directed poleward and up the gentle isentropic slope, and this may have provided the destabilization and organizational mechanism for the convection. The moistening resulting from this lifting is evident particularly for C1 (Figs. 5b, c). In the case of 16W, deep convection rapidly organized when the high θ_e and high moisture content of TCS-037 merged with similar thermodynamic characteristics at the leading edge of a frontal zone. Thus, mesoscale ascent due to baroclinic effects appeared to be an important ingredient for initiating or organizing deep convection and surface cyclogenesis.

The vertical shear in the cyclones studied herein was strongly modulated by cold lows and sub-synoptic-scale ridges in the upper troposphere, generally based at the tropopause. During the developments of C1 and C2, vertical wind shear was at least 6 ms^{-1} between 850 and 500 hPa. The modest thermal contrast that would accompany such shear at 30°N or 35°N is about 1 K per 300 km. This magnitude of thermal contrast rendered purely baroclinic development insignificant on time scales of a day. However, it was important for convective organization. Tropical cyclone 16W developed where there was a pronounced minimum in vertical shear averaged through the troposphere. For a brief time on 9 September the nascent disturbance found itself beneath anticyclonic vorticity flanked by two cyclonic anomalies, and in this location the vertical shear was small. In this case, weak vertical-shear and organized ascent were important for the remnant of TCS-037 to intensify while maintaining tropical characteristics.

Cyclone intensification in each of the three cases studied herein was favoured by conditions that were clearly transient. This contrasts with development in the deep tropics where even climatological mean conditions are relatively favourable. The transient nature of favourable conditions was also reflected in the relatively short period of intensification and subsequent weakening or extratropical transition. Especially in the case of 16W, the entire life cycle of a TC was compressed into a period of less than three days.

The fleeting nature of mesoscale developments such as those studied herein raises the question of predictability of these events. The ECMWF ensemble system (Leutbecher and Palmer, 2008) provides a basis for assessing the degree to which each mesoscale cyclone is predictable. In Fig. 19,

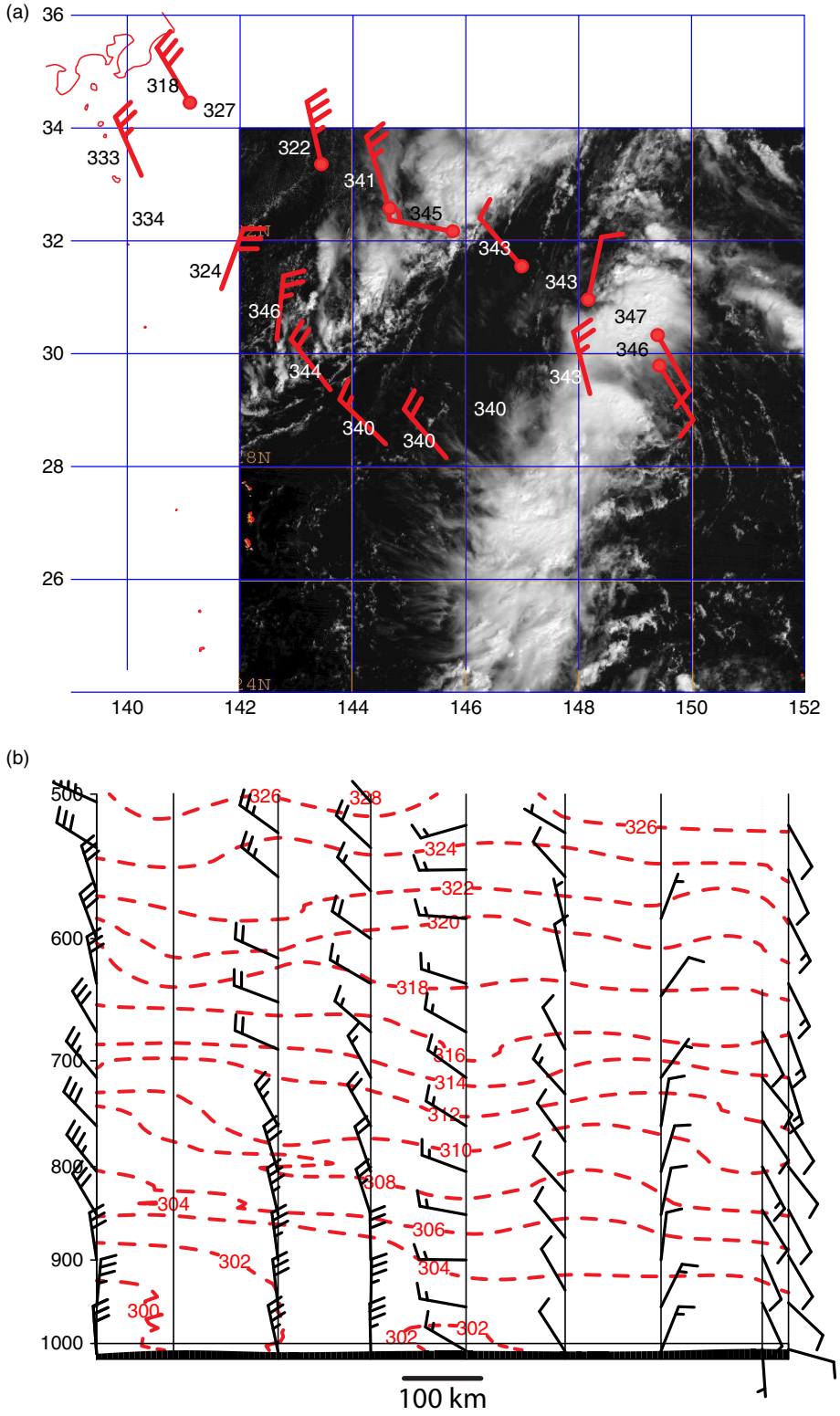

Fig. 17. (a) Winds at 850 hPa, time–space corrected and relative to movement of TCS037 (toward 315° at 5.5 ms^{-1}) and 850 hPa equivalent potential temperature (K) valid 0000 UTC 09 September superposed on GOES visible image for 2330 UTC 08 September; (b) cross section at 0000 UTC 09 September oriented from northwest (left) to southeast showing virtual potential temperature (K) and system-relative winds from soundings indicated by red dots in (a).

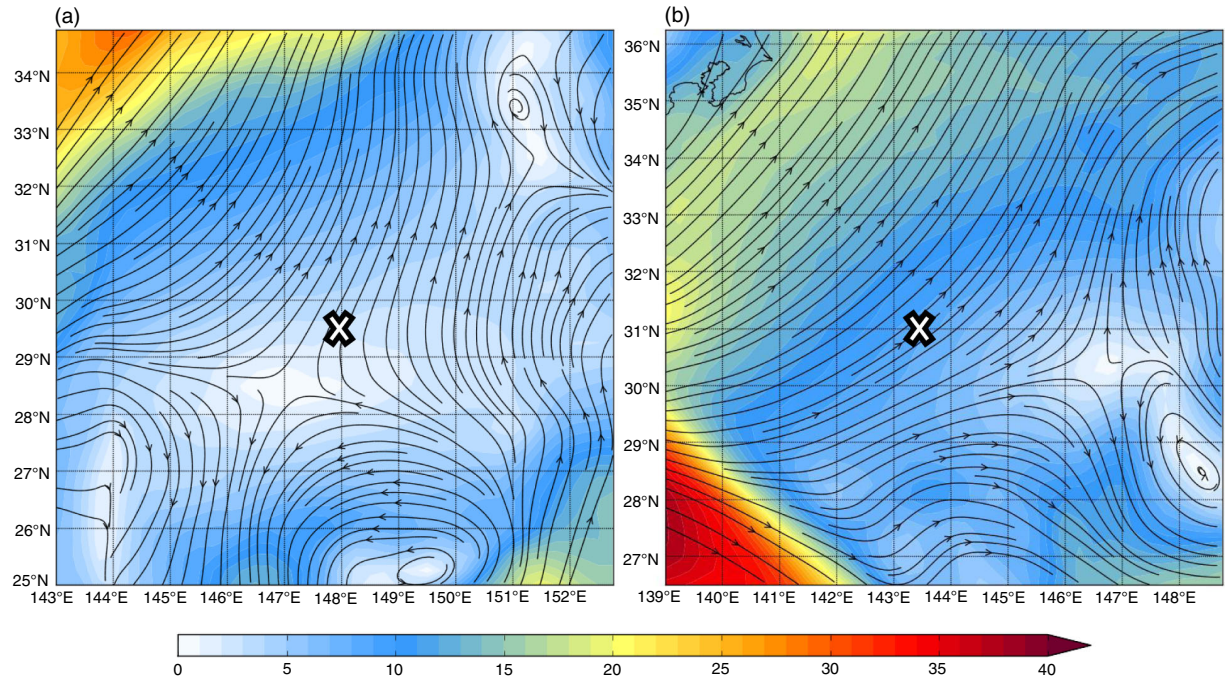

Fig. 18. Vector shear, depicted as streamlines and shear magnitude (m/s), in the layer from 850 to 200 hPa from the ECMWF analysis valid 12 UTC (a) 9 September and (b) 10 September. Disturbance has been removed prior to shear computation. Location of 16W is indicated by the white 'X'.

the 75th percentile of the distribution of vorticity at each grid point among the 51 ensemble members is shown. The ensemble mean vorticity and the 75th percentile agree qualitatively. It turns out that the ensemble has low predictive skill for the events at 96 h. At this time range, only a few members depict cyclonic vorticity in the correct region for C1 and 16W. A similar picture is true for the 72 h lead-time, although at this point there is a much stronger signal for 16W. The 72 h forecasts for 16W were initialized at 0000 UTC 9 September as convection began to organize. Dropsondes from the Falcon were included into the ECMWF data assimilation system, so this signal may reflect the addition of those observations.

By 48 h, C1 has a good representation in the ensemble, but C2 still has a weak signal, perhaps in part due to uncertainty in the position of the cyclone. Only at 24 h is there a relatively clear signal of C2. We should point out that these predictability estimates for C1 and C2 may be slightly optimistic compared to mesoscale marine cyclones in general owing to the additional observations that were deployed into TCS-025 on 27 and 28 August, many of which were assimilated by ECMWF.

The broader context for mesoscale cyclogenesis of the nature studied herein is the rich spectrum of phenomena that occur when intense deep convection is accompanied by high moisture contents and modest vertical wind shear. Rapid spinup of tropical cyclones due to bursts of convection organized by vertical shear is well documented (Davis and Bosart, 2003; Eastin et al., 2005; Molinari and Vollaro, 2010; Dolling and Barnes, 2012). Similarly, subtropical cyclones (Evans and Guishard, 2009) can also develop rapidly in sheared environments. These events are atypical among cases of tropical cyclogenesis in the deep tropics for which environments with weak wind shear are more favourable. For disturbances at higher latitudes, the co-existence of weak but persistent ascent governed by balanced (essentially quasi-geostrophic) processes with high moisture content and vertical shear characterizes pathways to tropical cyclones (McTaggart-Cowan et al., 2008). It is reasonable to expect that such baroclinic factors could also give rise to a variety of mesoscale marine cyclones that never achieve tropical cyclone status.

An important consideration for generating a strong tropical cyclone is that a sequence of organized convective events must occur, and remain close to the cyclone centre. A single burst can generate a weak TC from a depression, or a hurricane from a weak TC, but the presence of dry air in sheared environments that characterizes the subtropics and higher latitudes renders this difficult to achieve. Far more likely is the negative influence of dry air in sheared flow that disrupts the vertical circulation of the storm and moves the sustained deep convection farther from the centre (Riemer et al., 2010). The disruption and the

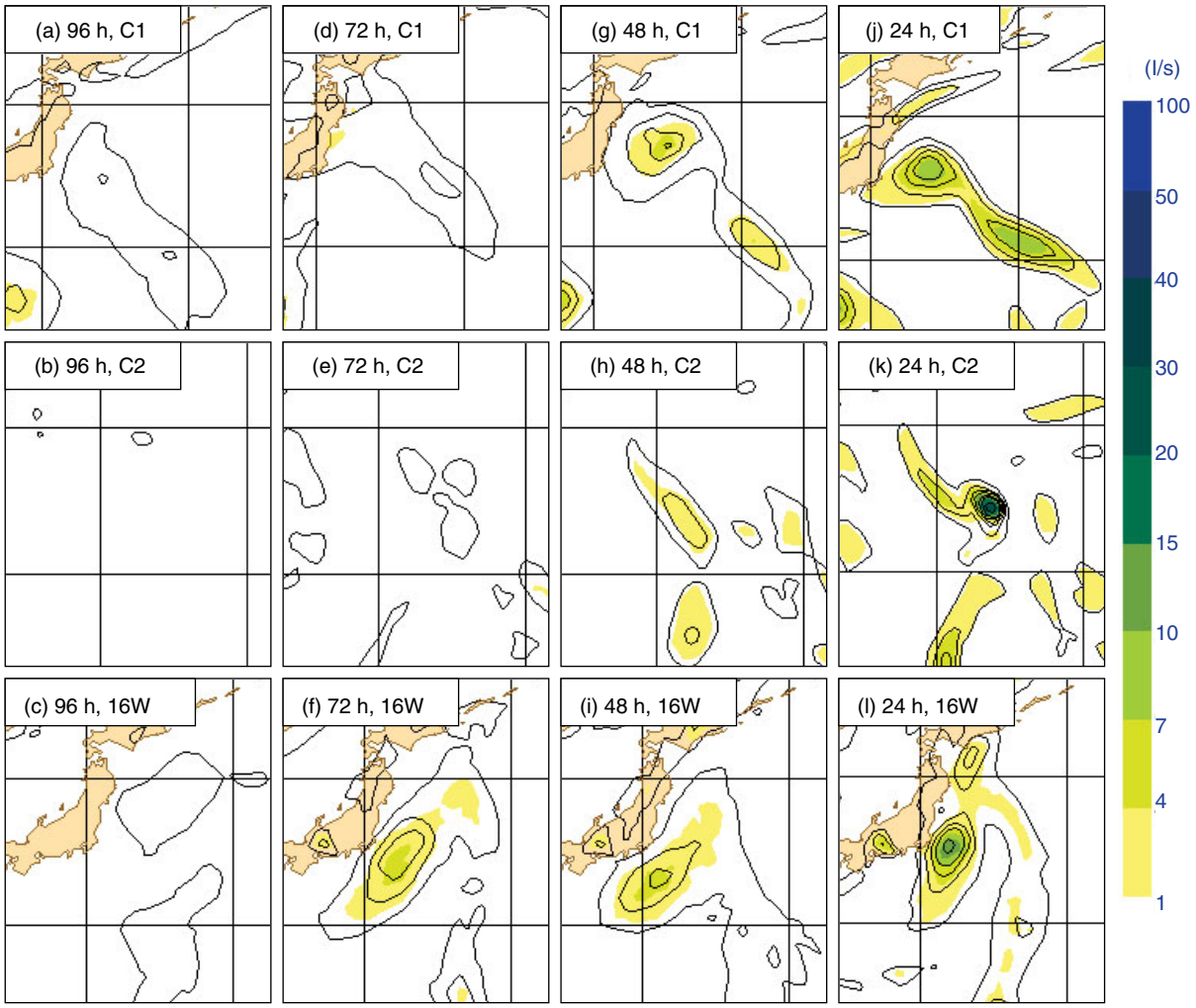

Fig. 19. Ensemble mean vorticity (contour interval 10–5 s^{-1}) and vorticity occurring in at least 75% of members (coloured as in Fig. 1). Top row: forecasts valid 00 UTC 31 August; middle row: forecasts valid 12 UTC 2 September; bottom row: forecasts valid 00 UTC 12 September.

asymmetry caused by shear, coupled with increasing baroclinicity at higher latitudes, gives rise to the asymmetries that characterize the extratropical transition process. Perhaps because mesoscale vortices of modest strength are not particularly resilient to shear or deformation, the entire life cycle of mesoscale cyclones such as those studied here is relatively short compared to well-developed tropical cyclones.

A logical next step in studying mesoscale cyclone developments would be a climatological analysis of the fate of remnants of tropical disturbances over the Western Pacific, both those that later attain TC status and those that do not. The Atlantic basin is known for its varied pathways to TC formation (McTaggart-Cowan et al., 2008), but analogous paths have yet to be quantified for the Pacific basin.

While we have distinguished mesoscale cyclone formation studied herein from TC formation in the deep tropics, the common theme is the emergence of a convective heating profile that favours vorticity and circulation increases at the surface. In the deep tropics, this is accomplished mainly by quasi-persistent convection embedded in a dynamically isolated rotating structure (the 'pouch' as coined by Dunkerton et al., 2009). This process is usually gradual and requires several convective cycles. However, we suggest that the presence of mesoscale lifting from baroclinic effects can produce a similarly favourable scenario in which weak isentropic lifting results in a nearly saturated condition that reduces the drying effect of downdrafts and favours near-surface convergence potentially resulting in a rapid vorticity increase. Numerical simulations without a

parameterization of deep convection are necessary to test this idea.

6. Acknowledgments

Data used in this study were collected as part of the THORPEX Pacific Asian Regional Campaign (TPARC). The DLR Falcon aircraft mission was led by Martin Weissmann and sponsored by an international consortium from Germany (DLR, Forschungszentrum Karlsruhe), the United States (National Science Foundation), Japan (Japan Meteorological Agency), Korea (National Institute of Meteorological Research) and Canada (Environment Canada). The role of the United States Navy and the National Center for Atmospheric Research's Earth Observing Laboratory (NCAR EOL) for campaign and data management is acknowledged. The authors also wish to thank Pat Harr of the Naval Postgraduate School in Monterey, California for his leadership of TPARC and numerous helpful discussions regarding the cyclone milieu in the Western Pacific. The authors acknowledge Julian Quinting for his assistance with shear computations and graphics, and Simon Lang for contributing numerous ECMWF-model-based graphical products to the TPARC web site (http://catalog.eol.ucar.edu/tparc_2008/index.html). Funding was received from the German Research Council projects PANDOWAE (FOR896) and from the Helmholtz Foundation ATMO Program. We gratefully acknowledge ECMWF for provision of the Year of Tropical Convection data set. The authors also wish to thank David Ahijevych of NCAR for assisting with the analysis of dropsonde and scatterometer data.

References

Atlas, R., Hoffman, R. N., Leidner, S. M., Sienkiewicz, J., Yu, T.-W. and co-authors. 2001. The effects of marine winds from scatterometer data on weather analysis and forecasting. *Bull. Amer. Meteor. Soc.* **82**, 1965–1990.

Bartels, D. L. and Maddox, R. A. 1991. Midlevel cyclonic vortices generated by mesoscale convective systems. *Mon. Wea. Rev.* **119**, 104–118.

Boettcher, M. and Wernli, H. 2012. A 10-year climatology of diabatic Rossby waves in the Northern Hemisphere. *Mon. Wea. Rev.* DOI: http://dx.doi.org/10.1175/MWR-D-12-00012.1.

Chakraborty, A. 2010. The Skill of ECMWF Medium-Range Forecasts during the Year of Tropical Convection 2008. *Mon. Wea. Rev.* **138**, 3787–3805.

Conzemius, R. J., Moore, R. W., Montgomery, M. T. and Davis, C. A. 2007. Mesoscale convective vortex formation in a weakly sheared moist neutral environment. *J. Atmos. Sci.* **64**, 1443–1466.

Davis, C. A. 2010. Simulations of subtropical cyclones in a baroclinic channel model. *J. Atmos. Sci.* **67**, 2871–2892.

Davis, C. A. and Bosart, L. F. 2003. Baroclinically induced tropical cyclogenesis. *Mon. Wea. Rev.* **131**, 2730–2747.

Davis, C. A. and Galarneau, T. J., Jr. 2009. The vertical structure of mesoscale convective vortices. *J. Atmos. Sci.* **66**, 686–704.

Davis, C. A., Snyder, C. S. and Didlake, A. C., Jr. 2008. A vortex-based perspective of eastern Pacific tropical cyclone formation. *Mon. Wea. Rev.* **136**, 2461–2477.

Dolling, K. and Barnes, G. M. 2012. Warm core formation in tropical storm Humberto (2001). *Mon. Wea. Rev.* **140**, 1177–1190. DOI: http://dx.doi.org/10.1175/MWR-D-11–00183.1.

Dunkerton, T. J., Montgomery, M. T. and Wang, Z. 2009. Tropical cyclogenesis in a tropical wave critical layer: easterly waves. *Atmos. Chem. Phys.* **9**, 5587–5646.

Eastin, M. D., Gray, W. M. and Black, P. G. 2005. Buoyancy of convective vertical motions in the inner core of intense hurricanes. Part II: case studies. *Mon. Wea. Rev.* **133**, 209–227.

Evans, J. L. and Guishard, M. P. 2009. Atlantic subtropical storms. Part I: diagnostic criteria and composite analysis. *Mon. Wea. Rev.* **137**, 2065–2080.

Hennon, C. C., Helms, C. N., Knapp, K. R. and Bowen, A. R. 2011. An objective algorithm for detecting and tracking tropical cloud clusters: implications for tropical cyclogenesis prediction. *J. Atmos. Oceanic Technol.* **28**, 1007–1018.

Jones, S. C., Harr, P. A., Abraham, J., Bosart, L. F., Bowyer, P. J. and co-authors. 2003. The extratropical transition of tropical cyclones: forecast challenges, current understanding, and future directions. *Wea. Forecasting.* **18**, 1052–1092.

Klein, P. M., Harr, P. A. and Elsberry, R. L. 2000. Extratropical transition of western north Pacific tropical cyclones: an overview and conceptual model of the transformation stage. *Wea. Forecasting.* **15**, 373–395.

Leutbecher, M. and Palmer, T. N. 2008. Ensemble forecasting. *J. Comput. Phys.* **227**, 3515–3539.

McTaggart-Cowan, R., Deane, G. D., Bosart, L. F., Davis, C. A. and Galarneau, T. J., Jr. 2008. Climatology of tropical cyclogenesis in the North Atlantic (1948–2004). *Mon. Wea. Rev.* **136**, 1284–1304.

Molinari, J. and Vollaro, D. 2010. Rapid intensification of a sheared tropical storm. *Mon. Wea. Rev.* **138**, 3869–3885.

Moore, R. W. and Montgomery, M. T. 2004. Reexamining the dynamics of short-scale, diabatic Rossby waves and their role in midlatitude moist cyclogenesis. *J. Atmos. Sci.* **61**, 754–768.

Parker, D. J. and Thorpe, A. J. 1995. Conditional convective heating in a baroclinic atmosphere: a model of convective frontogenesis. *J. Atmos. Sci.* **52**, 1699–1711.

Raymond, D. J., López-Carrillo, C. and López Cavazos, L. 1998. Case studies of developing east Pacific easterly waves. *Q. J. R. Meteorol. Soc.* **124**, 2005–2034.

Raymond, D. J., Sessions, S. L. and López Carrillo, C. 2011. Thermodynamics of tropical cyclogenesis in the northwest Pacific. *J. Geophys. Res.* **116**, D18101, DOI:10.1029/2011JD015624.

Riehl, H. 1948. On the formation of Typhoons. J. *Meteor.* **5**, 247–265.

Riemer, M., Montgomery, M. T. and Nicholls, M. E. 2010. A new paradigm for intensity modification of tropical cyclones: thermodynamic impact of vertical wind shear on the inflow layer. *Atmos. Chem. Phys.* **10**, 3163–3188, 28060.

Sadler, J. C. 1976. A role of the tropical upper tropospheric trough in early season typhoon development. *Mon. Wea. Rev.* **104**, 1266–1278.

Waliser, D. E. and Moncrieff, M. 2008. *Year of Tropical Convection (YOTC): The YOTC Science Plan*. WCRP-WWRP/THORPEX International Initiative WMP/TD-1452, 26 pp.

Wernli, H., Dirren, S., Liniger, M. A. and Zillig, M. 2002. Dynamical aspects of the life cycle of the winter storm 'Lothar' (24–26 December 1999). *Q. J. R. Meteor. Soc.* **128**, 405–429.